Hot Compression of Additively Manufactured Martensitic Stainless Steels

Shahriari, Ayda; Keshavarzi, Shokat; Forooghi, Foroozan; Keshavarzan, Mohsen; Hadadzadeh, Amir; Sanjari, Mehdi; Pirgazi, Hadi; Kestens, Leo A.I.; Shalchi Amirkhiz, Babak; Ofori-Opoku, Nana

DOI
10.1007/s11661-025-07879-1

Publication date
2025

Document Version
Final published version

Published in
Metallurgical and Materials Transactions A: Physical Metallurgy and Materials Science

Citation (APA)
Shahriari, A., Keshavarzi, S., Forooghi, F., Keshavarzan, M., Hadadzadeh, A., Sanjari, M., Pirgazi, H., Kestens, L. A. I., Shalchi Amirkhiz, B., Ofori-Opoku, N., Wells, M. A., & Mohammadi, M. (2025). Hot Compression of Additively Manufactured Martensitic Stainless Steels. *Metallurgical and Materials Transactions A: Physical Metallurgy and Materials Science*, *56*(9), 3900-3922. https://doi.org/10.1007/s11661-025-07879-1

Hot Compression of Additively Manufactured Martensitic Stainless Steels

AYDA SHAHRIARI, SHOKAT KESHAVARZI, FOROOZAN FOROOGHI,
MOHSEN KESHAVARZAN, AMIR HADADZADEH, MEHDI SANJARI,
HADI PIRGAZI, LEO A.I. KESTENS, BABAK SHALCHI AMIRKHIZ,
NANA OFORI-OPOKU, M.A. WELLS, and MOHSEN MOHAMMADI

Understanding the hot deformation behavior of metallic components produced *via* additive manufacturing (AM) is crucial, especially for applications in dynamic loads and high temperatures. This research examines the hot compression behavior of a martensitic precipitated hardened stainless steel, known as CX SS, produced through laser powder bed fusion (LPBF). Microstructural evolutions were examined on two sample types—as-built and heat-treated—subjected to hot compression at a constant 1 s^{-1} strain rate within the temperature range of 300 °C to 650 °C. The impact of microstructural features such as cellular solidification subgrains, nanoscale NiAl precipitates, and the austenite reversion transformation on dynamic recovery (DRV) and dynamic recrystallization (DRX) as mechanisms of restoration is explored using electron backscattered diffraction (EBSD) techniques. A comparison between two sample types revealed that the presence of cellular solidification substructure in the as-built samples delays the restoration mechanism compared to heat-treated samples. Furthermore, LPBF CX specimens in the as-built state and after heat-treatment process exhibit nearly identical deformation behavior at temperatures above 450 °C. This identical deformation behavior is associated with the partial or complete destruction of cells in the as-built samples and the dissolution of NiAl particles in heat-treated ones. The dynamic softening mechanism primarily stems from DRV and partial DRX. Although discontinuous dynamic recrystallization (DDRX) was alleviated in heat-treated samples, the as-built CX SS also showed softening mechanism in form of continuous dynamic recrystallization (CDRX) accompanied by DDRX. A constitutive equation of Arrhenius model, including Zener–Hollomon parameters, evaluated strain accumulation during hot deformation, identifying regions prone to shear bands (SBs), microcracks, and voids.

https://doi.org/10.1007/s11661-025-07879-1

I. INTRODUCTION

PRECIPITATION-HARDENABLE stainless steels represent a class of stainless steels known for their high strength, excellent toughness, sufficient corrosion resistance, and ease of fabrication. Moreover, they are cost-efficient metallic components when compared to titanium alloys.[1] The emergence of nanoscale precipitates in such alloys represents a notable strategy to enhance their mechanical properties. These precipitates

---

AYDA SHAHRIARI, FOROOZAN FOROOGHI, MOHSEN KESHAVARZAN, and MOHSEN MOHAMMADI are with the Marine Additive Manufacturing Centre of Excellence (MAMCE), University of New Brunswick, Fredericton E3B 5A3, Canada. Contact e-mail: ashahria@unb.ca SHOKAT KESHAVARZI is with the Marine Additive Manufacturing Centre of Excellence (MAMCE), University of New Brunswick and also with the Department of Physics, Faculty of Science, University of New Brunswick, Saint John E2L 4L5, Canada. AMIR HADADZADEH is with the Marine Additive Manufacturing Centre of Excellence (MAMCE), University of New Brunswick and also with the Department of Mechanical Engineering, University of Memphis, Memphis, TN 38152, MEHDI SANJARI and BABAK SHALCHI AMIRKHIZ are with the Marine Additive Manufacturing Centre of Excellence (MAMCE), University of New Brunswick and also with the CanmetMATERIALS, Natural Resources Canada, 183 Longwood Road South, Hamilton L8P 0A5, Canada. HADI PIRGAZI is with the Department of Electromechanical, Systems and Metal Engineering, Ghent University, 9052 Ghent, Belgium. LEO A.I. KESTENS is with the Department of Electromechanical, Systems and Metal Engineering, Ghent University and also with the Department of Materials Science and Engineering, Delft University of Technology, 2628 CD Delft, The Netherlands. NANA OFORI-OPOKU is with the Department of Materials Science and Engineering, Brockhouse Institute for Materials Research, McMaster University, Hamilton L8S 4L7, Canada. M.A. WELLS is with the Department of Mechanical and Mechatronics Engineering, University of Waterloo, Waterloo N2L 3G1, Canada.

Manuscript submitted November 21, 2024; accepted June 15, 2025.

not only play a considerable role in promoting mechanical performance but also impede grain growth to a certain extent, thereby enhancing both strength and toughness.[2,3]

CX stainless steel (CX SS) is a high-performance martensitic precipitation-hardening stainless steel primarily strengthened by nanoscale NiAl particles. It is specifically designed for the fabrication of intricately shaped parts through additive manufacturing (AM) techniques, notably the metallic AM technique of laser powder bed fusion (LPBF). Components made from CX stainless steel (CX SS) hold significant potential applications in industrial sectors such as aerospace, injection molding, nuclear sectors, and petrochemical sections.[4]

Additive manufacturing (AM) processes, particularly the laser powder bed fusion (LPBF) technique for fabricating metallic components, are in high demand across various industries due to their flexibility in producing complex geometries and their significant cost-effectiveness as well as reduction in the number of post-processing steps.[5,6] Nevertheless, the creation of a hierarchical microstructure, comprising internal boundaries, cellular solidification/subgrain structures, and chemical segregations, arises from the intensely localized melting, significant temperature gradient, and rapid solidification front velocity characteristic of LPBF.[7] This unique microstructure also leads to pronounced anisotropy in both the microstructure and mechanical properties.[8,9] Consequently, LPBF structures exhibit microstructural length scales from nanometers to sub-millimeters, distinguishing them from counterparts produced *via* conventional methods.[10]

Moreover, achieving the desired mechanical strength and toughness in the CX SS family of martensitic precipitation-hardening stainless steels fabricated by conventional methods involves conducting solution annealing and subsequent aging processes. These processes lead to the precipitation of nanoscale intermetallic compounds, such as NiAl.[11] However, studies indicated that the mechanical behavior of AM components under static conditions is comparable to, or even exceeds, that of both wrought materials and post-heat-treated AM components.[12,13] Accordingly, the unique microstructural features in the as-built components fabricated by AM methods can result in higher mechanical strength compared to their post-heat-treated counterparts. In stainless steel produced using the LPBF method, the evolution of local misorientation across cellular walls contributes to a high dislocation density in the as-built samples, leading to increased strength relative to annealed samples.[14]

Additionally, it is noteworthy that the synergistic effects of the thermomechanical conditions during the operation of AM components still lag behind those of their traditionally manufactured counterparts.[15] Subjecting LPBF parts to hot deformation conditions, such as those encountered in hot compression tests, can yield crucial insights into their flow behavior during hot formation. Additionally, it provides valuable information about dynamic recovery (DRV) as restoration processes and dynamic recrystallization (DRX) as another mechanism, which influence the softening behavior of components. Consequently, dynamic recovery (DRV) is likely to be activated in high stacking fault energy (SFE) metallic components, such as ferritic stainless steels, where dislocations can readily cross-slip, promoting recovery over recrystallization.[16] Furthermore, when strain hardening, coupled with recovery, reaches a point where it cannot accommodate additional stationary dislocations, and the critical strain is attained, DRV ceases, and DRX becomes the principal mechanism responsible for the softening behavior. Three different mechanisms of DRX that could influence the softening behavior of metallic structures are briefly summarized[17–19]:

- *Discontinuous dynamic recrystallization* (*DDRX*) this mechanism functions through a process of nucleation and growth, where new strain-free grains nucleate and grow at the expense of regions rich in dislocations.
- *Continuous dynamic recrystallization* (*CDRX*) this mechanism lacks a distinct nucleation phase; instead, the gradual increase in low-angle grain boundary (LAGB) misorientations leads to the evolution of new grains.
- *Geometric dynamic recrystallization* (*GDRX*) this mechanism occurs under high strain conditions, typically around 5 to 10 s^{-1}, where grains undergo fragmentation, resulting in the formation of new grains during deformation.[20]

Additionally, there is no clear distinction between these three DRX behaviors, and transformations between them occur depending on various deformation conditions and material states.[21,22] Furthermore, second phases in the form of the particles influence the recrystallization in various ways, either delaying or accelerating the process. This phenomenon is contingent on the size and spatial arrangement of the particles.[23] Typically, particles larger than 1 μm tend to facilitate recrystallization through particle-stimulated nucleation (PSN), whereas smaller particles ranging from approximately 10 to 300 nm slow down or impede the recrystallization process.[24] It has also been reported that precipitate-promoted DRX usually occurs with a small number of precipitates, whereas a hindering effect is observed when there is a large number of precipitates.[25] Furthermore, within the LPBF process, in-situ heat-treatment effects are active, particularly in the form of DRV and DRX. These processes occur due to the repeated heating and cooling cycles, which induce significant movement of the melt pool. Such conditions can increase the density of dislocations, leading to the formation of dislocation walls that evolve into substructure boundaries and eventually form low-angle grain boundaries (LAGBs). As stress accumulates beyond a critical threshold, LAGBs can continue to absorb dislocations, promoting DRX.[26,27] Additionally, the heat generated by laser scanning can penetrate previously solidified layers, creating heat-affected zones (HAZ) that significantly influence the microstructure and subsequent DRV/DRX processes. It has also been shown that the high cooling rates during the first two thermal cycles can lead to the formation of a highly deformed cellular microstructure. Therefore, during the third thermal cycle, DDRX and CDRX may be activated, contributing to grain refinement in LPBF-fabricated metallic components.[28,29] Furthermore, the formation of overlapping regions due to hatch spacing during laser scanning affects the activation of softening mechanisms in solidified microstructures. This interaction influences DRV/DRX processes in previously solidified regions, as observed in Ti alloys and austenitic stainless steels.[30–34] In other words, the multiple thermal cycles inherent in the LPBF process, along with in-situ softening processes, induce a combined thermal–mechanical effect, which should also be accounted for when metallic components undergo subsequent hot deformation. Consequently, complexities arise from the interactions among the distinctive microstructural features developed within the LPBF process, precipitation of nanoscale NiAl particles during the solution annealing and aging process, and the dynamic restorative mechanisms that take place during hot deformation conditions.

It is also known that thermomechanical parameters, including strain rate and temperature, influence flow behavior by affecting microstructural features and the mechanisms beyond softening.[35] Additionally, the flow behavior of metallic components during hot deformation processes can be predicted using constitutive equations. Numerous studies have focused on the hot deformation behavior of metallic alloys, leading to the proposal of several constitutive equations, such as the Arrhenius model with Zener–Hollomon parameters,[36] the Johnson–Cook model,[37] the Zerilli–Armstrong model,[38] and artificial neural network models (ANN).[39] These models have been employed to predict flow stresses of alloys during hot deformation processes. The Arrhenius model, as a widely used phenomenological constitutive equation, is favored for its fewer material constants and its ease of establishment and calibration. The Zener–Hollomon (Z–H) model, which has been modified to incorporate strain compensation, accounts for the effects of strain on material constants and the coupling between temperature and strain rate, thereby improving prediction accuracy.[40]

To gain a deeper understanding of how the development of various microstructural features affects the flow behavior of LPBF components during hot deformation, this study proposes accurate constitutive equations based on the phenomenological model to effectively predict flow stress and deformation behavior of LPBF components during the hot deformation process. The objective of this study is to identify the correlation between the distinctive microstructural features formed during the LPBF process, post-heat treatment, and softening mechanisms happening during high temperature deformation. The results of this study provide valuable insights for predicting and designing microstructure–property relationships tailored to industrial applications. This is particularly crucial in hot deformation conditions, where the synergistic effects of temperature and applied strain could significantly impact the operational lifespan of metallic components fabricated by LPBF process.

II. EXPERIMENTAL

A. *Material and Hot Compression (HT) Measurements*

EOS Stainless-steel CX powders, fabricated by gas atomization method, were poured into an EOS M290 laser powder bed fusion (LPBF) machine to build rod shape specimens with dimensions of 12 mm in diameter and 120 mm in length. The powders were of spherical morphology with a volume-equivalent sphere diameter of $d_{90} = 42.37\ \mu$m. The chemical composition of the powder is as follows: C = 0.05 wt pct, Cr = 12.48 to 13 wt pct, Ni = 8.4 to 10 wt pct, Al = 1.32 to 2 wt pct, Mo = 1.46 to 1.7 wt pct, Mn = 0.37 to 0.4 wt pct, Si = 0.12 to 0.4 wt pct, and Fe = balance content. The rod-shaped samples were printed vertically, with their long axes aligned parallel to the Z-axis, as depicted in Figure 1(a). The fabrication process parameters of the rod samples are also illustrated in Figure 1(a).

Cylindrical compression samples, measuring φ 6.67 mm × 10 mm, were machined from the as-built samples with their long axes aligned parallel to the build direction (BD), as illustrated in Figure 1(a). Some of the samples underwent two thermal processing cycles corresponding to the H986 heat treatment for the family group of 13.8 PH Mo stainless steel. The first cycle involved a solution annealing at 900 °C for a soaking time of 1 hour, followed by air cooling. The second cycle comprised an aging process, where precipitation reactions led to the formation of nanoscale NiAl precipitates. During this aging process, the material was maintained at 530 °C for 3 hours and subsequently air cooled. A schematic of the solution annealing and aging as the post treatment is presented in Figure 1(b). The estimation of solid-state phase transformations during heating was also measured using dilatometry tests conducted during continuous heating at a rate of 5 °C/s, as shown in Figure 1(c). The $\Delta L/L_0$ *vs.* temperature plot was taken from dilatometry test at a heating rate of 5 °C/s for the LPBF CX SS, indicating the precipitation and the martensite-to-austenite transformation (A_{C1}) temperatures.

The LPBF CX SS specimens are considered in two states: as-built and after applying the solution annealing and aging process (Heat-treated state). The as-built samples were denoted as B samples, while the heat-treated samples were referred to as H samples. These specimens were then subjected to isothermal uniaxial hot compression (HT) tests. Thermocouple wires were attached to the surface of the compression specimens at the midpoint to monitor and regulate the temperature of deformation during HT. The thermal–mechanical simulation testing system, Gleeble® 3500, was utilized for conducting HT experiments. The specimens were heated to the deformation temperature at a rate of 5 °C/s, maintained at the deformation temperature for 30 seconds for uniform temperature distribution, then

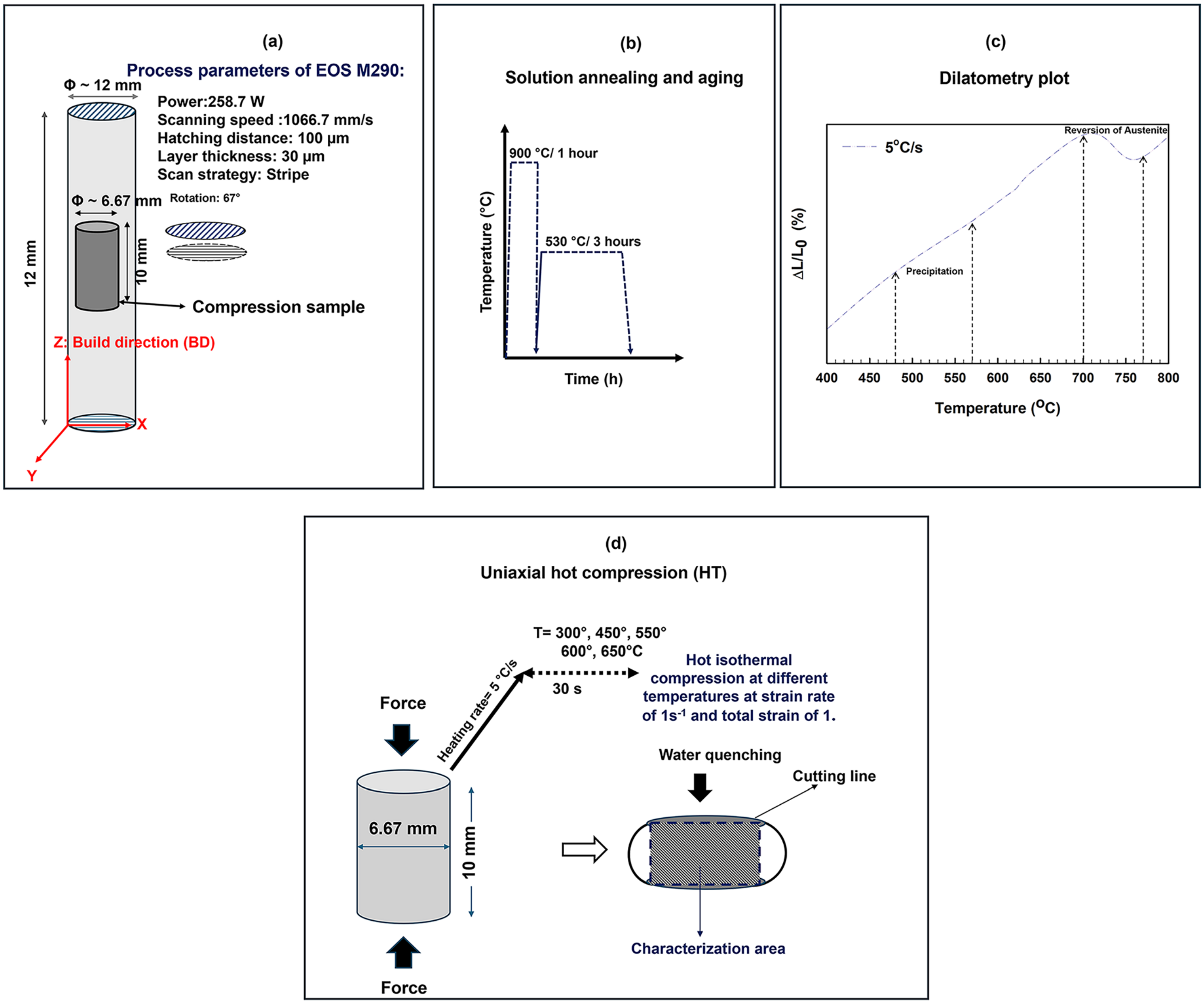

Fig. 1—(*a*) A schematic illustrating the LPBF process parameters, the fabricated CX SS sample, and the specimen prepared for hot compression, (*b*) the heat-treatment process applied to LPBF CX SS samples, (*c*) the corresponding dilatometry plot, and (*d*) an illustrative representation of the hot compression procedure and cutting plane for microstructural characterization.

deformed and rapidly cooled with water to maintain the microstructure, as depicted schematically in Figure 1(d). Deformation was carried out until a final true strain of 1 was reached at temperatures of 300 °C, 450 °C, 550 °C, 600 °C, and 650 °C, with strain rates set at 1 s^{-1}. However, some samples failed before reaching this strain. To minimize friction during hot deformation, a carbon-based lubricant was applied to the ends of the samples.

B. *Microstructural Characterization*

The samples subjected to thermomechanical treatment were sliced longitudinally and analyzed for their microstructure using an optical microscope (OM), scanning electron microscope (SEM), and an electron backscattered diffraction (EBSD) system. A schematic indicating the areas selected for microstructural characterization is presented in Figure 1(d). For OM and SEM observations, the preparation of samples was performed based on standard metallographic procedures, followed by etching with Beraha's tint etchant.[41] Grinding and polishing were performed on the surface of the samples to prepare them for EBSD analyses. Accordingly, a high-resolution field emission gun scanning electron microscope (HR-FEGSEM, FEI QUANTA 450) outfitted with TSL-OIM software was used for the EBSD observations. Step sizes of 0.5 and 0.2 μm were selected to scan areas of approximately 0.25 mm^2, with the sample tilted at 70 deg. In TEM investigations, an FEI Tecnai Osiris TEM was employed, operated at an accelerating voltage of 200 kV, equipped with a high current X-FEG electron source which in combination with Super-X EDXS detector equipped was with quad Silicon Drift Detectors

(SDDs) allowing high count rates for creating elemental maps.

III. MODELING: DEFORMATION ANALYSES

It is well understood that the inherent mechanisms during hot deformation have a close correlation with the microstructural features, which can be reflected in values of characteristic stresses such as peak stress.[42] Accordingly, variations in microstructural features also affect the activation energy (Q) for hot compression, suggesting a good agreement between the activation energy for hot deformation and diffusion activation energy. Prior research has suggested that certain microstructural characteristics may enhance the activation energy required for deformation, resulting in a higher degree of softening mechanisms such as recrystallization.[42–44] On the other hand, the relationship between flow stress and deformation conditions is also elucidated through Arrhenius equations, aiming to explain how peak stress depends on temperature of deformation process and strain rate:

$$\dot{\varepsilon} = A_1\sigma^{n_1}\exp\left(-\frac{Q}{RT}\right), \quad [1]$$

$$\dot{\varepsilon} = A_2\exp(\beta\sigma)\exp\left(-\frac{Q}{RT}\right), \quad [2]$$

$$\dot{\varepsilon} = A(\sinh(\alpha\sigma))^{n}\exp\left(-\frac{Q}{RT}\right), \quad [3]$$

where $\dot{\varepsilon}$ represents strain rate (s^{-1}), the universal gas constant (8.31 J/mol/K) is shown by R, T denotes the absolute temperature (K), activation energy for the hot deformation is denoted by Q in kJ/mol, and σ represents the flow stress (MPa) for a given stain. The material constants are A_1, A_2, A, n_1, α, and n. Also, $\alpha = \frac{\beta}{n}$. Using the equations provided above, both temperature of deformation and strain rate can be regarded as contributing factors in the Zener–Hollomon (Z) parameter formulation:

$$Z = \dot{\varepsilon}\exp\left(\frac{Q}{RT}\right). \quad [4]$$

Taking the natural logarithm on both sides of Eqs. [1] through [3] and finding the slopes of the graphs of $\ln\dot{\varepsilon} - \ln\sigma$, $\ln\dot{\varepsilon} - \sigma$, and $\ln\dot{\varepsilon}$-$\ln(\sinh(\alpha\sigma))$ by substituting the values of the flow stress and corresponding strain rate at specific strains, and applying linear regression, all material constants can be deduced. Furthermore, the constants values of both B and H samples of CX stainless steel fabricated by LPBF process are substituted into Eq. [3] to obtain the constitutive equation for B and H samples, as shown in Eqs. [5] through [6] in Table I.

Then, the flow stress (σ) is expressed as a function of the Zener–Hollomon parameter, considering the hyperbolic law definitions for both B and H conditions as described in Eqs. [7] and [8], respectively:

$$\sigma = \frac{1}{0.0166}\ln\left\{\left(\frac{Z}{3.28\times10^{11}}\right)^{\frac{1}{4.63}} + \left[\left(\frac{Z}{3.28\times10^{11}}\right)^{\frac{2}{4.63}} + 1\right]^{\frac{1}{2}}\right\}, \quad [7]$$

$$\sigma = \frac{1}{0.011}\ln\left\{\left(\frac{Z}{2.54\times10^{11}}\right)^{\frac{1}{3.73}} + \left[\left(\frac{Z}{2.54\times10^{11}}\right)^{\frac{2}{3.73}} + 1\right]^{\frac{1}{2}}\right\}. \quad [8]$$

The constitutive equations for hot-deformed CX SS samples are derived under the assumption that the stress exponent and activation energy remain constant regardless of the deformation conditions. However, differences in the constant values, particularly the activation energy between the as-built and heat-treated states, suggest that these parameters may be influenced by factors like temperature, applied stress, and the deformed sample's microstructure. Furthermore, the change in activation energy from the as-built state to the heat-treated condition could reflect the strong impact of microstructural features on the hot compression behavior and relaxation processes.[45]

The accuracy of the deformation constitutive equation was evaluated by calculating the error between the calculated flow stress (σ_f) and the measured flow stress (σ_m) at various strains and shown in Figure 2(a). The maximum error was found to be 6.9 pct with a standard deviation of 8.8 pct. These results confirm that the suggested equation provides a reasonable estimation of the hot deformation behavior of CX SS fabricated by LPBF process in the as-built state and heat-treated condition. Additionally, the measured stress–strain values during the hot deformation process for both B specimens and H ones, along with the calculated values using the constitutive models mentioned above, are compared and presented in the following sections. These comparisons confirm that the hyperbolic sine function model calculated in this research accurately predicts the hot deformation characteristics of LPBF CX samples in both conditions.

Finite element simulations of hot compression were also performed using the Arrhenius constitutive model integrated into the ABAQUS/Standard software. Figure 2(b) illustrates the axisymmetric configuration of the fabricated cylindrical specimens, featuring an initial length of 10 mm and a radius of 3.3 mm. The upper and bottom punches were treated as 2D analytical rigid bodies. To ensure optimal mesh quality during substantial deformations, an adaptive mesh size was implemented, particularly near the punches, allowing the mesh to move independently of the material. The workpiece was discretized using a 4-node bilinear axisymmetric quadrilateral (CAX4R) with reduced integration and hourglass control, resulting in a mesh size of 5088 elements. Hot compression of CX SS material typically involves metal plastic forming, where elastic

Table I. The Constitutive Equations for LPBF Parts, As-built Samples and Those Subjected to Heat Treatment

Condition	Constitutive Equation
As-built (B Samples)	$\dot{\varepsilon} = 3.28 \times 10^{11}[\sinh(0.0166\sigma)]^{4.63}\exp\left[-\frac{411.4\times10^{3}}{RT}\right]$ (5)
Heat-Treated (H Samples)	$\dot{\varepsilon} = 2.54 \times 10^{11}[\sinh(0.011\sigma)]^{3.73}\exp\left[-\frac{387\times10^{3}}{RT}\right]$ (6)

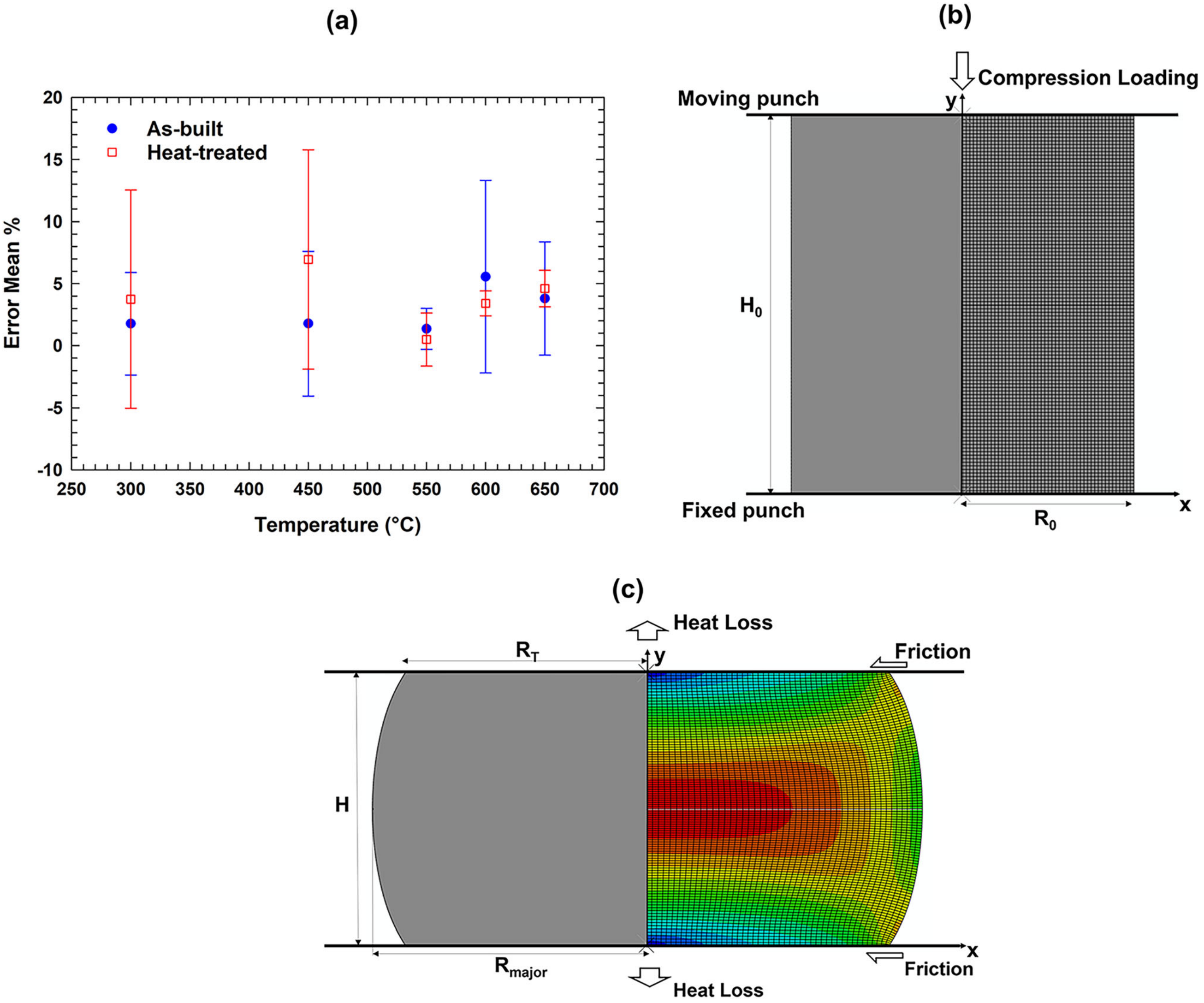

Fig. 2—(*a*) Mean of errors obtained from the measured and calculated flow stress values at certain strains, (*b*) initial dimensions and compression loading setup for the finite element modeling of a cylindrical sample under uniaxial compression, and (*c*) real scenario illustrating barrel distortion caused by friction and temperature gradients in the finite element modeling.

deformation effects were disregarded. The strain rate correlates with the increase in temperature during hot deformation. Hot compression processes at high strain rates are conducted under adiabatic conditions, leading to a significant temperature rise in samples. Conversely, temperature variations due to deformation are minimal under low strain rates, maintaining an isothermal condition.[46] Throughout the compression process, the upper punch descended along the negative *Y*-axis direction, while the bottom punch remained stationary. Friction at the interface between the specimen and punch resulted in non-uniform plastic deformation, including the formation of a dead zone. Empirical evidence suggests that temperature and strain rate during the deformation affect the friction factor (m_f). Friction coefficients were specified at the interfaces between the workpiece and rigid punches as follows[47]:

$$m_f = \frac{(R/H)b}{(4/\sqrt{3}) - (2b/3\sqrt{3})}, \quad [9]$$

where the barrel parameter is shown by b and the height and average radius of the cylinder specimen after hot deformation is denoted by H and R, respectively, the barrel parameter b and average radius R is defined as follows:

$$b = 4\frac{\Delta R}{R}\frac{H}{\Delta H}, \quad [10]$$

$$R = R_0\sqrt{\frac{H_0}{H}}, \quad [11]$$

where ΔH and ΔR represent the reduction in height and the difference between the maximum radius and top radius of the cylinder parts after deformation. The friction factor is ascertained from Eqs. [9] through [11] using measurements of height, maximum radius, and top radius. However, accurately measuring the top radius post-deformation is challenging. Thus, approximating the barreled sample's profile with an arc of a circle allows for calculating the top radius using Eq. [12]:

$$R_T = \sqrt{3\frac{H_0}{H}R_0^2 - 2R_{\text{major}}^2}, \quad [12]$$

where R_{major} and R_T denote the maximum radius and top radius of cylinder part after compression process, as depicted in Figure 2(c). The constant friction factor of these tests was 0.11. Finally, the user-defined material subroutine UHARD is also employed to analyze effective strain, effective stress, and temperature distributions in the workpiece during hot compression, leveraging the reliable output provided by FEM for complex plastic forming processes. This subroutine is instrumental in addressing challenges related to predicting material behavior, especially in scenarios involving the nonlinear characteristics of hot-deformed materials. Implemented at all material calculation points, the UHARD subroutine continuously adjusts stresses and state variables dependent on the solution at the conclusion of each increment.

IV. RESULTS AND DISCUSSION

A. *Stress–Strain Rate Measurements*

The typical true stress–strain plots for the B and H samples are shown in Figures 3(a) and (b). Generally, it can be observed from Figures 3(a) and (b) that the flow stress decreases with an increase in deformation temperature. However, the as-built sample hot deformed at 450 °C (B_{450}) showed a higher flow behavior than the as-built sample hot deformed at 300 °C (B_{300}). Additionally, the amount of reduction in flow stress differs between the as-built hot-deformed samples and those that were hot deformed at the same temperatures as the heat-treated samples. Moreover, the flow response of the B and H samples converges after hot deformation at temperatures above 450 °C. These findings from the mechanical response of the as-built as well as the heat-treated specimens indicate that microstructural changes occur during the hot compression process. This results in the convergence of the mechanical behavior of both states at elevated temperatures. Additionally, the calculated true stress–strain values using the constitutive equations described previously are depicted in Figures 3(a) and (b) as solid lines. The comparison of the experimental stress–strain data with the calculated values at different temperatures under a strain rate of 1 s^{-1} revealed that the outcomes from the experiment closely match the predicted results, verifying the underlying mechanism on which the developed constitutive equations for the LPBF CX stainless steel samples have been founded (Figure 2(a)).

The peak stress values related to the hot-deformed samples are presented in Figure 3(c). The values presented at room temperature (RT) actually represent the ultimate strength (σ_{US}) obtained from previous tensile tests on as-built CX SS samples and those exposed to heat-treatment process, as depicted in our previous study.[48] The remaining values represent the peak stresses (σ_P) measured from the true stress–strain curves measured during HT tests performed on both states of the CX SS alloy. The highest stress was attained from the CX SS sample after solution annealing and aging treatment, following a tensile test performed at RT. This value is equivalent to the ultimate tensile stress. Additionally, Figure 3(c) presents the ultimate tensile strength (σ_{US}) of the as-built LPBF CX SS sample, as determined from the tensile test at RT. The σ_{US} values for both the as-built and heat-treated samples are labeled as RT in Figure 3(c). As shown in Figure 3(c), there is a substantial difference of about 675 MPa between the values of σ_{US} for heat-treated and as-built samples. Also, the peak stress (σ_P) values obtained from the stress–strain plots related to hot compression decrease with the rise in deformation temperatures for both states deformed samples (B and H samples), converging at deformation temperatures of 550 °C, 600 °C, and 650 °C. Consequently, a reduction in the highest stress for hot-deformed samples was also observed compared to those RT samples, suggesting the involvement of softening mechanisms attributed to dynamic recovery (DRV) and dynamic recrystallization (DRX). Furthermore, a comparison of the σ_P values for hot-deformed samples at different temperatures, as well as a comparison between σ_P and σ_{US}, suggests that the H samples exhibit greater susceptibility to softening mechanisms than the B samples. This is evidenced by a more pronounced reduction in peak stress in the H samples compared to the B samples (trend indicated by the black arrow in Figure 3(c)). Additionally, the differences in σ_P values between B_{550}, B_{600}, and B_{650} and their corresponding H samples (H_{550}, H_{600}, and H_{650}) are about 51, 3, and 7 MPa, respectively. This indicates that the hot deformation flow behavior of the

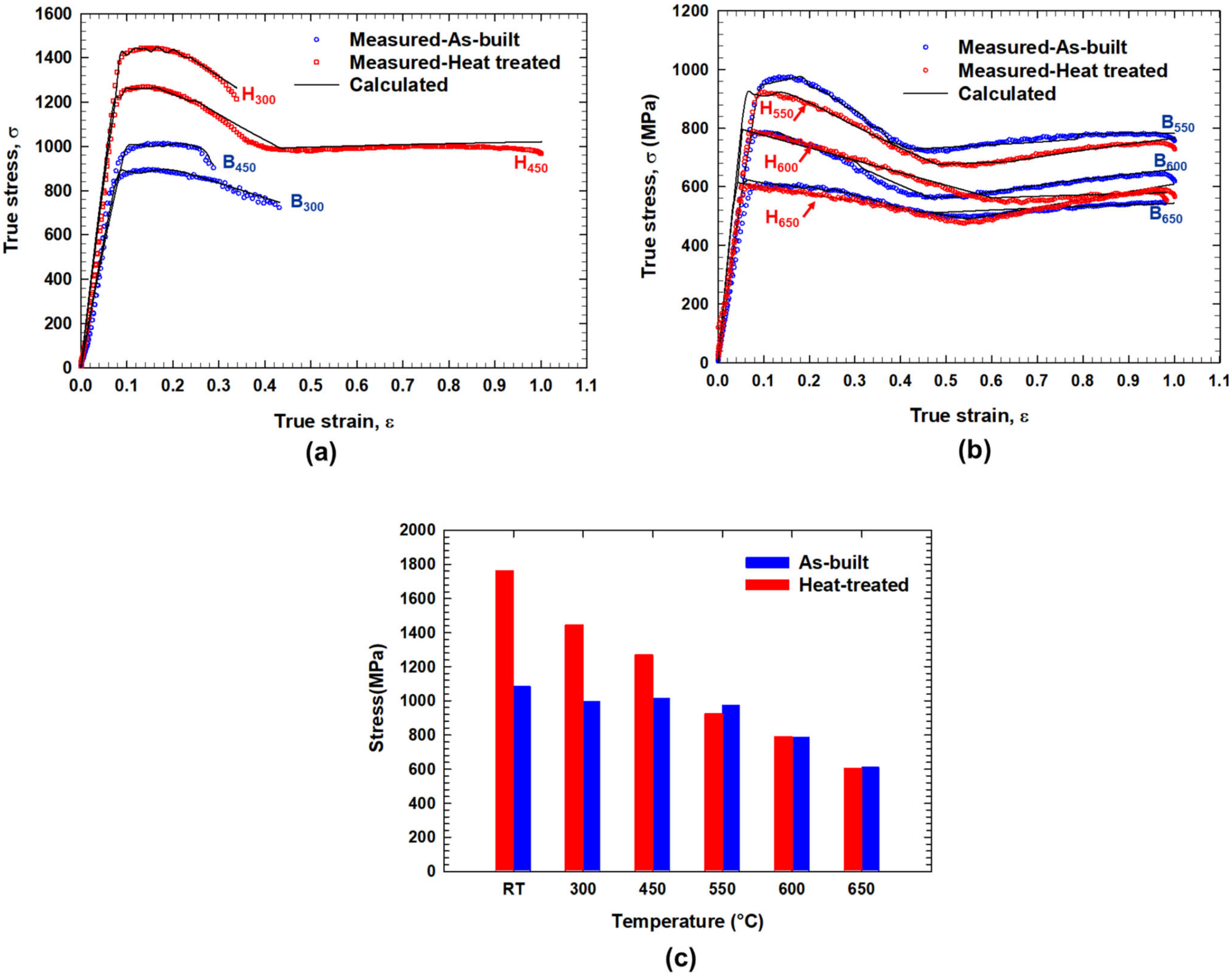

Fig. 3—True stress–strain plots obtained after hot compression tests at different temperatures for the (*a*) as-built (B) and (*b*) Heat-treated (H) specimens. Solid lines in the true stress–strain plots are corresponding calculated values from the constitutive formula (*c*) ultimate strength/peak flow stress obtained after deformations at RT and different deformation temperatures for the as-built and heat-treated LPBF CX SS.

as-built samples at 550 °C, 600 °C, and 650 °C is nearly identical to that of their heat-treated counterparts deformed at the same temperatures.

B. *Flow Localization Behavior and Microstructure*

Figure 4 presents OM/SEM images of undeformed and deformed specimens, along with image quality (IQ) maps for selected samples. Additionally, the locations of the OM-photographed areas in the hot-compressed samples are schematically marked and shown in Figure 4(a). The letters noted in the top left corner of each image are associated with the OM-photographed position. The images of the as-built specimen without the hot deformation process (B_0) exhibit a hierarchical structure, including meltpools characterized by micrograins containing a forest of solidification cells elongated in the direction of growth (Figure 4(a)). It is crucial to emphasize that the cellular microstructure observed in the as-built state is not a result of thermodynamic equilibrium, and this structure tends to undergo decomposition during the post-heat-treatment process.[49,50] Following the solution annealing and aging process (H_0), the microstructure appears to be homogeneous, devoid of any discernible melt pools or scan tracks (Figure 4(a)). Additionally, the cellular structures linked to the microsegregation of alloying elements under a particle accumulation structure (PAS) mechanism during the rapid solidification of the LPBF process have disappeared.[50] It is evidenced by micrographs pertaining to the H_0 sample (Figure 4(a)).

The SEM images taken from B_{450} and B_{550} also show the presence of cellular structures, as shown in Figures 4(b) and (c). Despite the elevation in deformation temperature, there is also a trend of fine cells converging into larger subgrains, yet they remain confined within the larger micrograins. Evidence of partially decomposed cellular structures becomes apparent in the SEM image associated with the B_{550} (marked with red arrows, Figure 4(c)). The SEM picture of the B_{650} reveals the absence of cellular structures under a hot deformation temperature of 650 °C (Figure 4(d)).

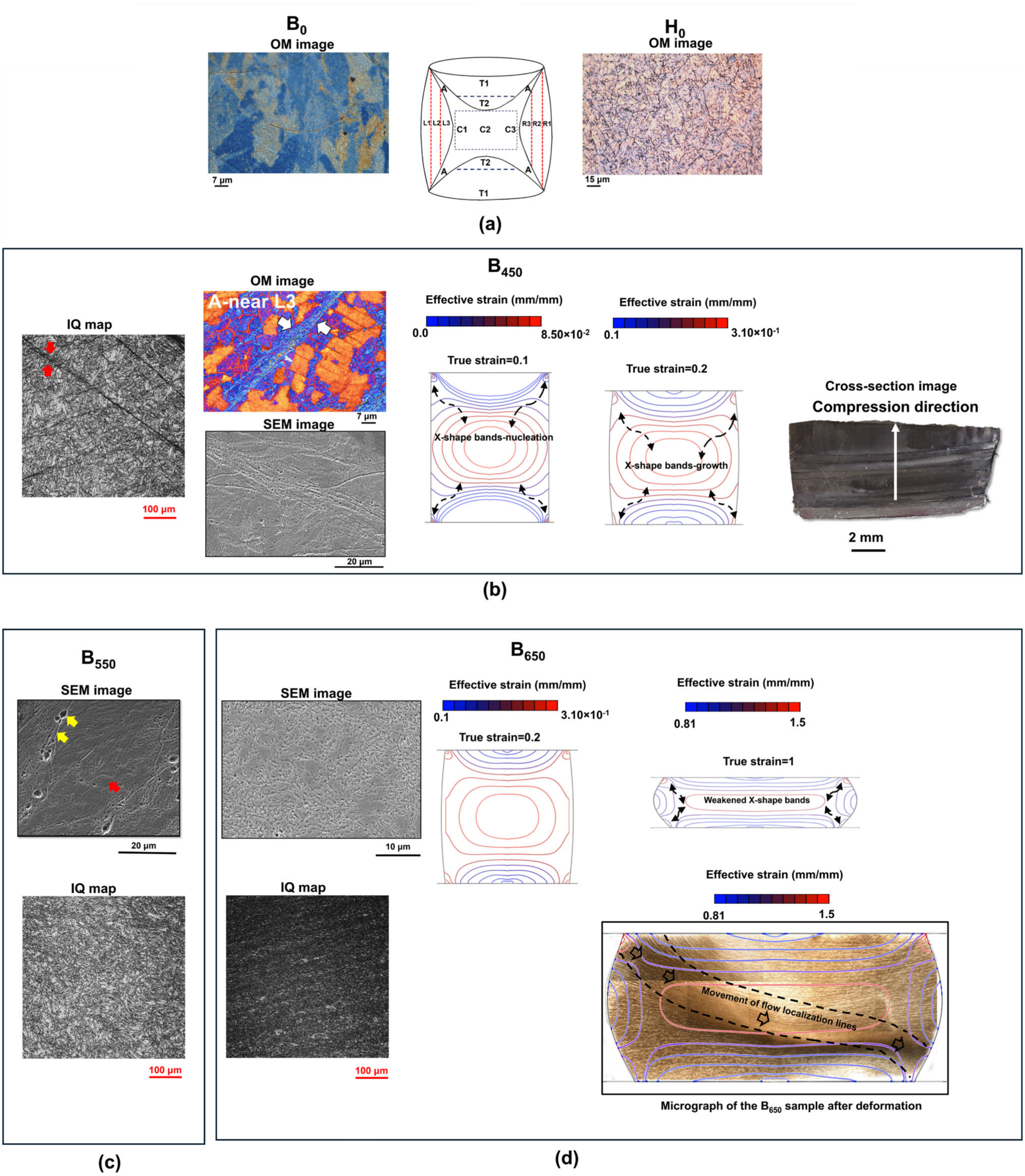

Fig. 4—(*a*) OM micrographs of LPBF CX SS samples without hot deformation, showing the positions identified as T1, T2, L1, L2, L3, R1, R2, R3, C1, C2, C3, and A in the axial section for microstructural analysis, (*b*) OM/SEM/IQ images of B$_{450}$, including its effective strain distribution during hot compression and a cross-sectional image of its deformation, (*c*) SEM/IQ images of B$_{550}$, and (*d*) SEM/IQ images of B$_{650}$, along with its effective strain distribution during hot compression and a cross-sectional image of its deformation. (*e*) OM/SEM/IQ images of H$_{300}$, including its effective strain distribution during hot compression and a cross-sectional image of its deformation, (*f*) OM/SEM images of H$_{450}$, showing its effective strain distribution during hot compression and a cross-sectional image of its deformation, (*g*) OM/IQ images of H$_{650}$, along with its effective strain distribution during hot compression and a cross-sectional image of its deformation, (*h*) average grain size of all samples, (*i*) grain boundary character distribution (GBCD) of the as-built LPBF samples, and (*j*) GBCD of heat-treated LPBF samples (Color figure online).

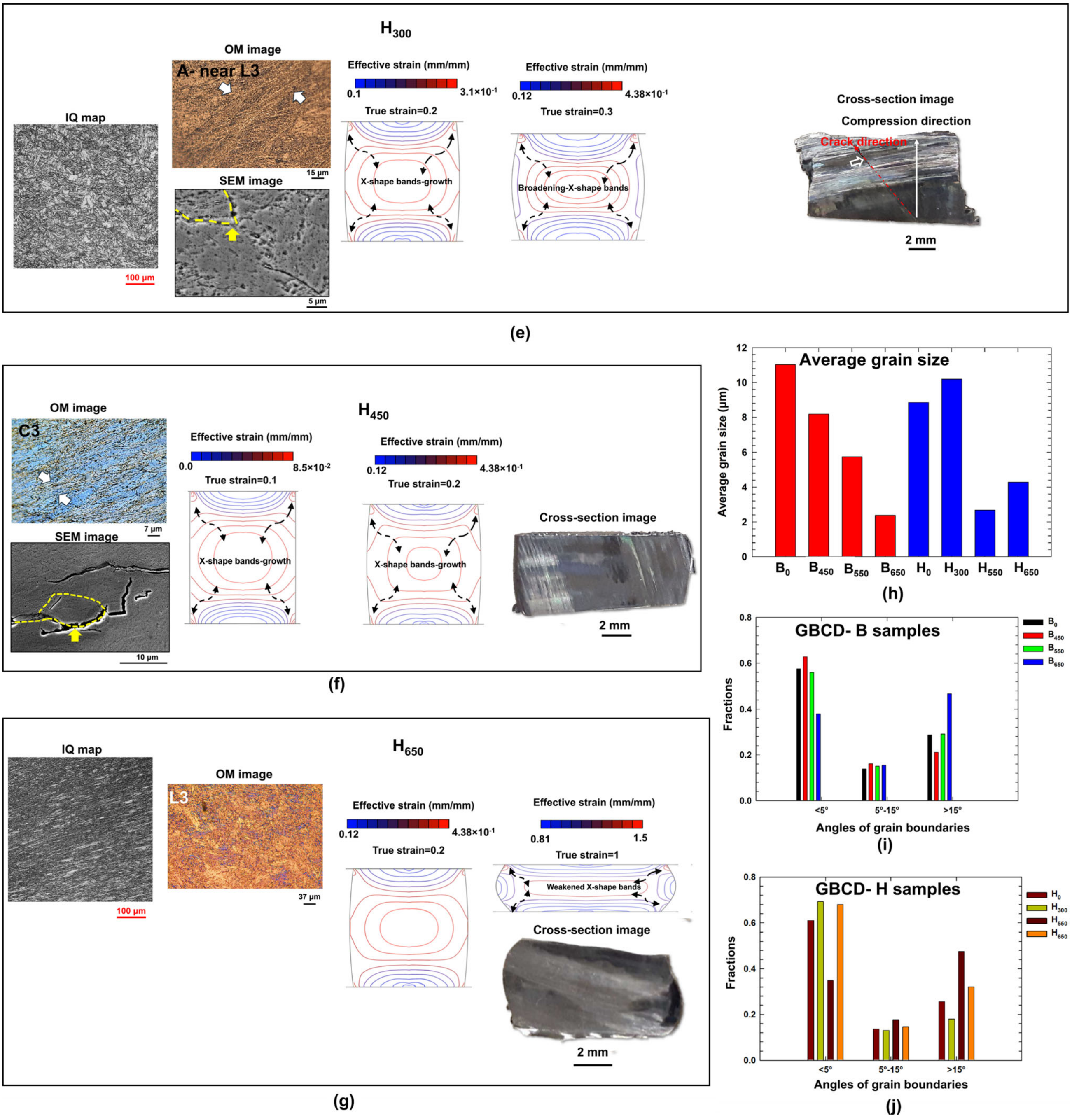

Fig. 4—continued.

Similar to the H_0 sample, heat-treated samples subjected to the hot deformation process exhibit no discernible traces of melt pools, scan tracks, or cellular microstructures, as observed in the OM/SEM images of H_{300}, H_{450}, and H_{650} shown in Figures 4(e) through (g).

Figure 4(b) also shows that hot deformation of the as-built LPBF specimens at 450 °C (B_{450}) resulted in the formation of regions of intense deformation represented by shear bands (SBs). These SBs are indicated by white arrows in the OM image and highlighted with red arrows in the IQ map (Figure 4(b)). Deformation at 550 °C and 650 °C resulted in a mixed microstructure featuring fine recrystallized regions within a matrix consisting of elongated, and coarser grains originated from the initial microstructure, as observed in IQ maps in Figures 4(c) and (d). Moreover, a comparison of the IQ image from B_{650} with that of the B_{550} sample suggests that the subsequent increase in the hot compression temperature has resulted in a greater volume fraction of recrystallized grains, consequently resulting in a finer structure compared to the B_{550} sample. A higher deformation temperature can promote dislocations' cross-slip, increase atomic diffusion, and raise the rate of subgrain boundary migration, as well as foster their coalescence. These phenomena are associated with DRX mechanisms.[51,52] The emergence of SBs, marked by white arrows in the OM images and resulting from flow instability, is also evident in the H_{300} and H_{450} samples, oriented at approximately 45 deg to the compression axis (Figures 4(e) and (f)). Upon further temperature increase, the indications of SBs diminish in H_{650} sample. Subsequent deformation in these samples leads to extensive recrystallization, as illustrated in the IQ maps of H_{650} and H_{300}. Finer grains are developed in H_{650} compared to H_{300}.

Furthermore, examination of images from B_{450}, H_{300}, and H_{450} samples suggests that the SBs are composed of fine grains formed through recrystallization. At high strain rates, the heat generated by plastic deformation over a short period causes a rapid rise in local temperature, which cannot be adequately dissipated. As a result, local deformation resistance decreases, intensifying further deformation and leading to dislocation accumulation. This contributes to the formation of SBs, often manifesting as adiabatic shear bands (ASBs) within the grain.[53] The localized temperature elevation within the SBs, coupled with a substantial accumulation of stored deformation energy, promotes a propensity for DRX within the bands. However, the newly formed DRX grains face a limitation in growth due to the rapid strain rate, preventing them from reaching their full potential size. Microcracks and voids were observed in all samples; however, microcracks and voids in B_{550}, H_{300}, and H_{450} samples are specifically highlighted with yellow arrows and dashed lines in SEM images in Figures 4(c), (e) and (f).

To better understand the formation of SBs in the hot-deformed samples, photographs of the cross sections of the B_{450}, H_{300}, H_{450}, B_{650}, and H_{650} samples after deformation are shown in Figure 4. These images are accompanied by their corresponding effective strain contours at strains of 0.1, and 0.2 for B_{450}; 0.2 and 0.3 for H_{300}; 0.1 and 0.2 for H_{450}; and 0.2, and 1 for B_{650} and H_{650} samples. The microstructural images in Figure 4, along with the corresponding effective strain contours, indicate that hot deformation of the specimens at temperatures of 300 °C and 450 °C tends to lead to the development of strain-localized areas and SBs appearing as approximately X-shaped bands. These bands intersect in the central region of the hot-compressed samples, as depicted schematically in Figure 4(a). However, these X-shaped SBs broadened, weakened, and eventually disappeared in hot-deformed samples at higher temperatures of 450 °C. Evidence of SBs was not detected in samples hot deformed at temperatures of 550 °C, 600 °C, and 650 °C. Accordingly, it seems that the degree of strain localization increases with decreasing temperature, indicating that the formation of SBs is sensitive to temperature. Moreover, the change in temperature also alters some microstructural features within the hot compression process, which could stimulate the formation of SBs, as these microstructural factors affect flow localization. A comparison between the effective strain distributions in the hot-compressed samples at 300 °C and 450 °C with those at 650 °C (Figures 4(b) and (d) and (e) through (g)) implies that, at the initial stages of deformation and with a 18 pct reduction in height (equal to strain $= 0.2$), a relatively higher gradient of effective strains forms X shapes in the samples deformed at low temperatures (B_{450}, H_{300}, and H_{450}). In contrast, the strain distribution is more uniform, with a smaller gradient and a rectangular shape indicative of uniform plastic deformation, in the samples deformed at higher temperatures (B_{650} and H_{650}).

Additionally, it can be estimated from the effective strain distribution contours that the initial strain localization for the formation of SBs tends to originate from the center and corners of the samples hot deformed at 300 °C and 450 °C. The micrographs taken from the hot-deformed sample also show that the initiation of microcracks occurs at positions "A" and "C," as illustrated in Figure 4(a). A superposition of the effective strain contours on the light micrograph of the flow line contours formed after hot deformation at 650 °C in the as-built state sample (B_{650}) is shown in Figure 4(d). Accordingly, the flow lines disclosed through macro-etching distinctly illustrate significant strain concentration at the center and along the roughly X-shaped bands, which start from the left and right corners and cross each other at the specimen's center. The contours of effective strain also confirmed the presence of the highest degree of strain in the center and the X-band areas of the specimen. Although fractures did not occur in the B_{650} sample, the flow lines indicate that the distribution of deformation penetrated deeper into the right section of the specimen along one branch of the X bands, oriented from the upper left corner, as marked with a dashed line in the light micrograph (Figure 4(d)). Therefore, it can be inferred that during the hot deformation of samples B_{300}, B_{450}, and H_{300}, one branch of the X-shaped SBs would be stronger than the other, resulting in asymmetrical deformation and fracture of these specimens. Accordingly, photographs of the cross sections of the fractured samples (B_{450}, H_{300}) shown in Figures 4(b) and (e) also revealed an asymmetrical deformation and traces of cracks in roughly X-shaped areas, as detected from the effective strain contours.

The presence of asymmetrical deformation is detected by measuring the final minor (R_{minor}) and major (R_{major}) diameters of the hot-compressed samples. The $R_{\mathrm{minor}}/R_{\mathrm{major}}$ ratio is approximately 0.5 and 0.7 for the B_{300} and B_{450} samples, respectively. This ratio reaches 1 when the B samples are hot compressed at 650 °C, indicating that a higher hot deformation temperature results in more symmetric deformation and a more uniform distribution of effective strain. Additionally, the $R_{\mathrm{minor}}/R_{\mathrm{major}}$ values are near 1 for the heat-treated samples, except for the H_{300} and H_{450} samples, which show values of 0.6 and 0.7, respectively. These findings confirm that the as-built samples have a higher tendency toward asymmetric deformation compared to the heat-treated ones. Asymmetric deformation was detected at 550 °C and 600 °C in B samples, while symmetric deformation was noted in H samples, which were hot deformed at 550 °C and 600 °C. The different tendencies in softening mechanisms could also affect the deviation in symmetrical deformation between the as-built samples and those subjected to post-heat treatment, resulting in a non-uniform distribution of effective strain and a tendency for flow localizations.

Intergranular cracks were also noted in SEM images of H_{300} and H_{450} samples (Figures 4(e) and (f)), marked with yellow dashed lines, suggesting that grain boundaries (GBs) in the heat-treated samples weaken and become prone to cracking. The deposition of dislocation slips at GBs in the heat-treated samples could contribute significantly to stress concentration, inducing the formation of voids and cracks at these grain boundaries. The presence of a cellular subgrain microstructure in the as-built state of LPBF samples, along with phase transformations such as the martensite-to-austenite ($\alpha_M \rightarrow \gamma$) reversion and the dissolution/precipitation of nanoscale intermetallic particles, introduces complexities that substantially influence the DRV and DRX phenomena.

Additionally, Figures 4(h) through (j) display the average values of grain size of B and H samples along with the corresponding Grain Boundary Character Distribution (GBCD) plots. The decrease in the value of average grain size of deformed B samples compared to the undeformed sample (B_0) is illustrated in Figure 4(h). However, in the heat-treated state, except for the H_{300} sample, the average value of grain size of the remaining specimens has reduced in comparison to H_0, with an increase in deformation temperature. Based on results from OM/SEM analyses and average grain size values (Figure 4(h)), it is possible to infer that regardless of the deformation conditions, the samples have experienced DRX, although to different degrees.

In comparison, the average grain size values (Figure 4(h)) suggest that hot deformation at 650 °C of the as-built sample led to the evolution of the finest grains. However, the deformation at 650 °C resulted in a decrease in grain size in H_{650} was not as pronounced as observed in B_{650} sample. Furthermore, analyzing the GBCD plots (Figure 4(i)) of the deformed B samples in contrast to the undeformed ones showed that the angle grain boundaries' fraction (AGB) < 5 deg, which could indicate strain accumulation, decreases with increasing in hot deformation temperature. Also, the highest fractions of AGB > 15 deg indexing high-angle grain boundaries (HAGBs) are also relieved for the samples with lowest average grain size, B_{650} and H_{550} (Figures 4(i) and (j)). The evolution of new recrystallized grains as well as grown recrystallized grains could be attributed to the formation of HAGBs, indicating a high degree of DRX could have occurred in the B_{650} and H_{550} samples. For all samples, the fraction of AGB between 5 and 15 deg is almost the same implying a lath martensitic structure as the primary phase in deformed and undeformed samples.

Examining the hot compression conditions and the effects of microstructural changes on softening mechanisms during hot deformation is crucial for understanding LPBF-fabricated samples, both in the as-built state and after heat treatment. The following results and discussion aim to provide insights into the role of microstructural features developed in LPBF CX SS and their evolution after heat treatment in influencing the hot compression behavior of martensitic stainless steel fabricated by LPBF.

C. *Microstructure Evolution: Softening and Cracking Mechanism*

An IQ map with presence of SBs in B sample deformed at 450 °C (B_{450}) is depicted in Figure 5(a). An enlarged view of the highlighted area with red dashed lines in Figure 5(a) is also presented as maps of inverse pole figure (IPF) in the building direction (IPF-BD) and grain boundary (GB) in Figure 5(b). SBs bands are also marked with black dashed lines in IPF map (Figure 5(b)). Here, accumulation of fine grains in the SBs bands is detectable as marked with dashed circles in IPF map of Figure 5(b). These fine grains exhibit a recrystallized structure with a more equiaxed morphology compared to the initial microstructure. The formation of serrated boundaries, the nucleation around grain boundaries (indicated by the white dashed circle), and subsequent evolution of a necklace-type structure (highlighted by the yellow dashed circle) suggest the occurrence of bulging mechanisms under discontinuous dynamic recrystallization (DDRX), as observed in Figure 5(b).

The corresponding GB map in Figure 5(b) suggests that the accumulation of low-angle grain boundaries (highlighted by green and red lines) is more prominent within the SBs in contrast to the remaining microstructure, confirming the localization of strain during hot deformation in these regions. Additionally, the IPF-BD map of the area marked with a white circle in Figure 5(b) is also magnified in Figure 5(c). The misorientation plots along arrows shown in nuclei DRX grain as Grain 1 and the Grain 2 which is surrounded with the DRX nucleus in IPF-BD map of Figure 5(c) are also shown in this figure. The plots represent point-to-point and point-to-origin misorientation profiles. In Grain 1, both point-to-point and point-to-origin misorientation values are lower compared to the deformed grain (Grain 2), indicating the release of accumulated strains in new DRX grains. Furthermore, the point-to-point misorientation exhibits a fluctuating low degree of misorientation, while the point-to-original profile demonstrates continuous elevation in Grain 2. This type of misorientation profile signifies the generation of geometrically necessary dislocations (GNDs) and strain gradient within the deformed grain. The formation of GNDs guarantees strain compatibility.[17,54]

A uniform network of fine recrystallized grains is evident in the IPF map derived from the B_{550} sample deformed at 550 °C (Figure 6(a)). As a result, consistent patterns of small recrystallized grains along the boundaries of the original grain structure can be observed. Furthermore, the microstructure depicted in Figure 6(a) is segmented into two areas by a white dashed line, representing the low DRX and high DRX regions. The accumulation of DRX grain networks is more pronounced in the High DRX area compared to the Low

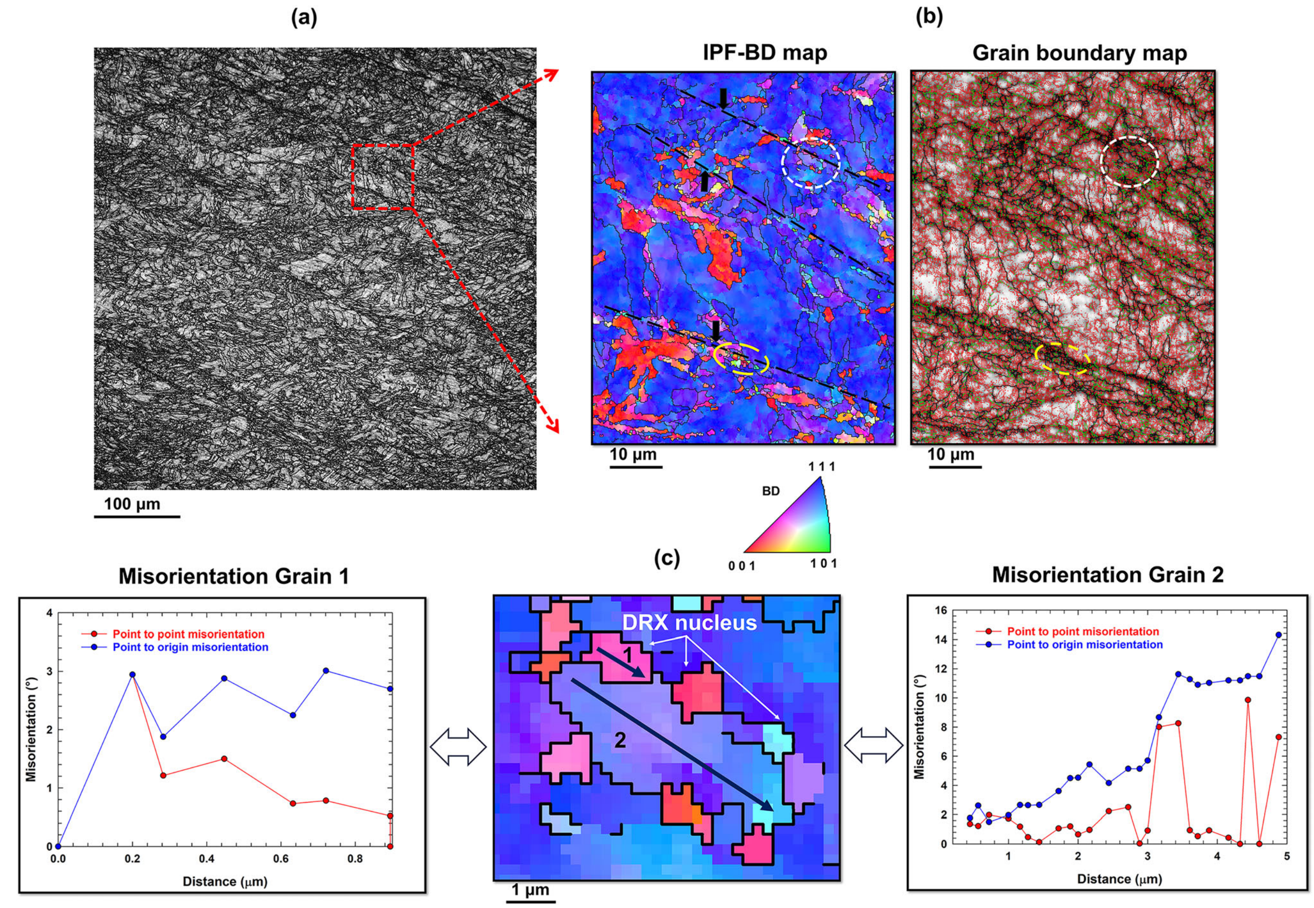

Fig. 5—EBSD maps of B_{450} sample, (*a*) IPF-BD map of a larger area, (*b*) IPF-BD and misorientation maps of the dashed rectangle marked in (a) (color code: red: AGB) < 5 deg, green: 5 deg < AGB < 15 deg and blue: HAGBs), and (*c*) IPF-BD of the white circle area shown in (b) with corresponding misorienting plots of grains 1 and 2 marked in (Color figure online).

DRX region. The branches of the structure display a favored alignment, seemingly associated with the direction of the highest resolved shear stress generated during the hot deformation process. Moreover, the corresponding aspect ratio map presented in Figure 6(b) affirms that the High DRX area is predominantly populated by green and red colors compared to the Low DRX region. This suggests that more equiaxed recrystallized grains are accommodated in the High DRX area compared to the Low DRX region. The variations in austenite fraction (depicted by green spots) are discernible from the phase maps obtained in sections of the Low DRX area and High DRX regions, as depicted in Figure 6(c).

As depicted in Figure 6(c), a higher austenite volume fraction is discernible in the High DRX area compared to the Low DRX region. This suggests that the formation of the reversed austenite phase within the hot compression process, known as the reversion of austenite, was influenced by the dynamic recrystallization of the matrix.[55] Moreover, the proportion of austenite was approximated to be around 14.6 pct from the EBSD measurements for the B_{650} sample, which underwent hot deformation at 650 °C, thereby confirming the concurrent occurrence of DRX and austenite reversion.

Subsequently, the development of recrystallization and the identification of potential sites for nucleation were explored by partitioning the EBSD maps using the Grain Orientation Spread (GOS) criterion of ≤ 1 deg for both the B_{650} and as-built sample (B_0), as illustrated in Figure 7. The white regions in the EBSD maps denote grains characterized by high internal local crystalline perfection and minimal lattice curvature, suggesting possible areas of recrystallization. Corresponding SE images are also provided adjacent to the EBSD maps in Figure 7. The SE picture of the B_{650} sample further validates the disappearance of cellular solidification structures. Additionally, some micro-sized grains lacking cellular subgrains are delineated by dashed black lines in the SE image of the B_{650} sample. The corresponding EBSD map of the B_{650} sample reveals the development of new fine grains characterized by low accumulations of red and green lines associated with LAGB of 2 to 5 deg and LAGB 5 to 15 deg, respectively. In contrast, the as-built sample without the hot deformation process (B_0) exhibited a cellular solidification structure, highlighted by dashed yellow lines in the SE image. Furthermore, the corresponding EBSD map of the B_0 sample illustrates a higher accumulation of low-angle grain boundaries (indicated by red and green

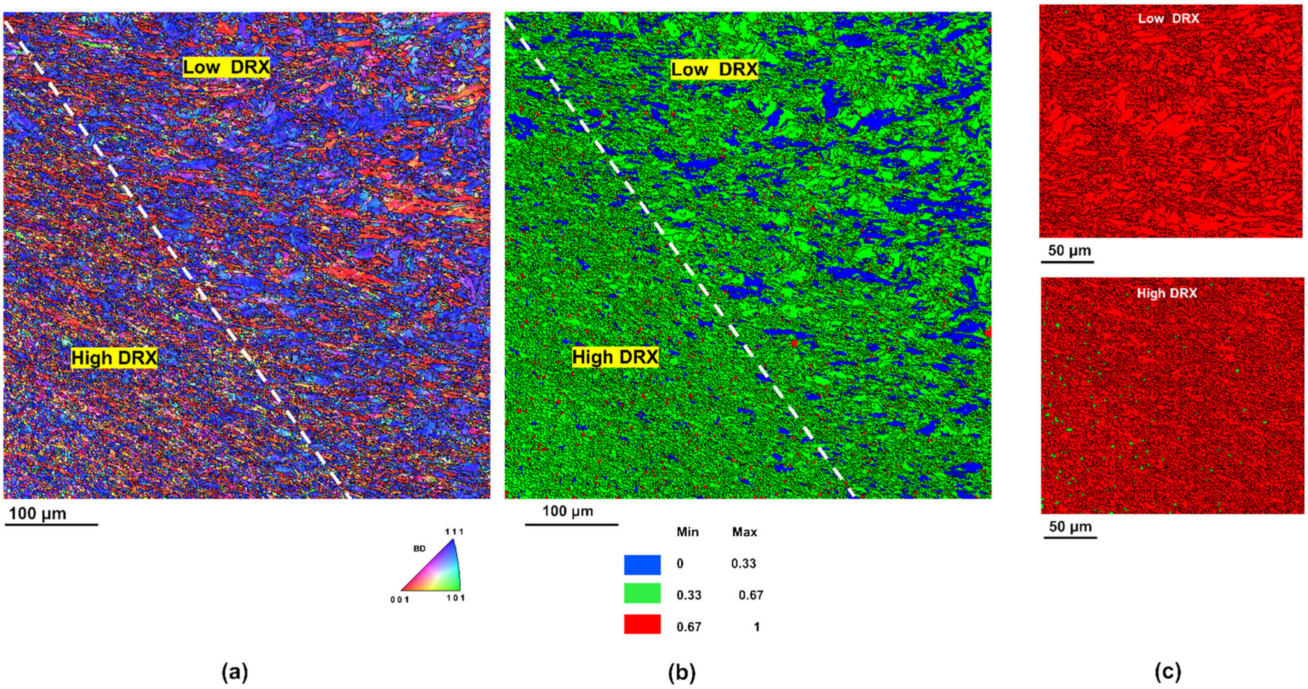

Fig. 6—EBSD maps for the as-built LPBF CX sample deformed at 550 °C (B_{550}), (*a*) IPF-BD map, (*b*) aspect ratio maps, and (*c*) corresponding phase maps of an area inside low DRX and high DRX (the red means martensite phase and green means austenite phase) (Color figure online).

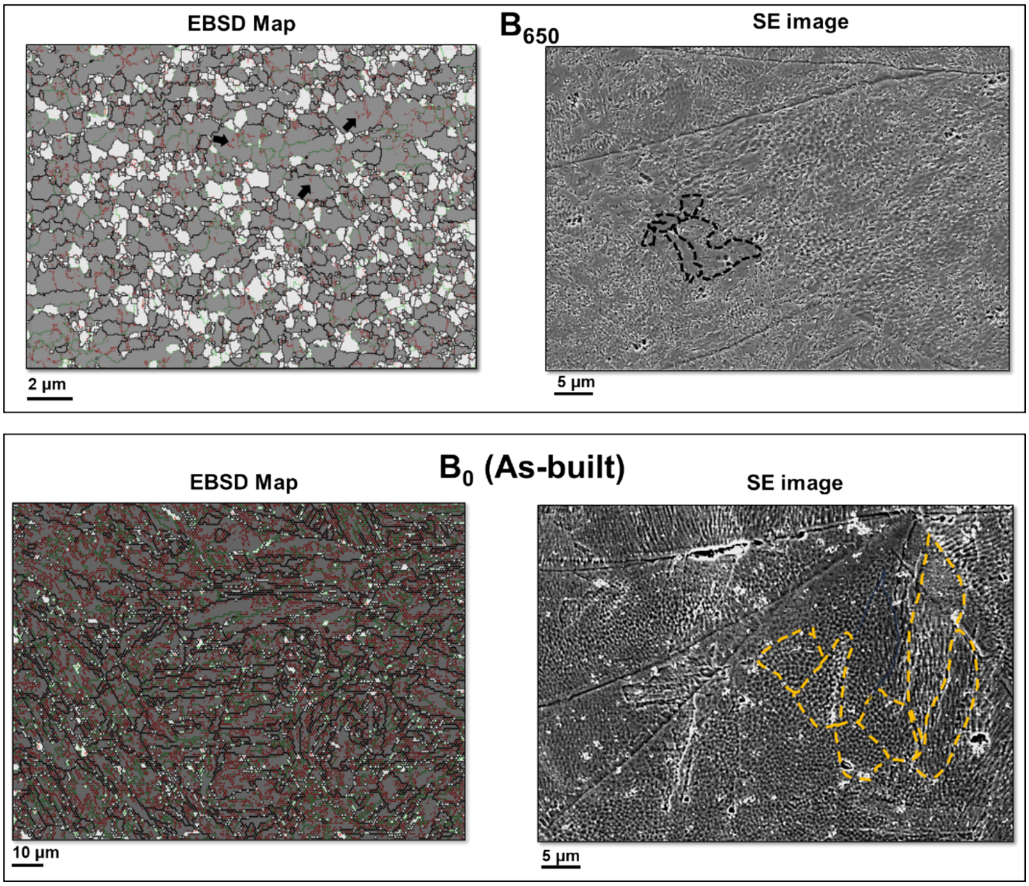

Fig. 7—EBSD maps of the partitioned microstructure with GOS ≤ 1 deg (withe area are recrystallized regions) and angle grain boundaries [boundary color code: LAGB (2 to 5 deg)-red; LAGB (5 to 15 deg)-green; HAGB (> 15 deg)-black] and SEM micrographs of the samples hot deformed at 650 °C (B_{650}) and sample without deformation (as-built, B_0) (Color figure online).

lines) compared to those observed in the B_{650} sample. The high accumulations of low-angle grain boundaries [LAGBs: (2 to 15 deg)] suggest the presence of a substructure, including the cellular solidification subgrains formed during rapid laser solidification. Consequently, the accumulation of LAGBs in B_{650} decreased compared to B_0, indicating the elimination of the cellular substructure after hot compression at 650 °C.

The cellular structures consist of dense cellular walls or boundaries created by entangled dislocations, surrounding regions devoid of dislocations. Additionally, the segregation of solute elements occurs along these cellular boundaries, potentially influencing their susceptibility to recovery and recrystallization. The presence of cellular solidification substructure could impede recrystallization due to solute drag resulting from the partitioning of elements at cell walls.[56] Hence, it is noteworthy that the cellular structures remain stable during the hot deformation process at temperatures below 650 °C, potentially influencing the kinetics of recovery and recrystallization. The reduction in grain size (depicted in Figure 4(h)) and the decrease in flow stress (σ_P) shown in Figure 3(a) for the as-built samples hot-deformed at temperatures below 650 °C, compared to the RT sample of B samples, are less than those calculated for the hot-pressed heat-treated samples at the same temperature, compared to the RT sample of H samples. This confirms that the restoration mechanisms in the initial built state are more sluggish compared to those in the heat-treated condition.

The EBSD map of B_{650} also reveals incomplete LAGBs, indicated by arrows in Figure 7, within grains possessing high-angle grain boundaries (HAGBs), a distinguishing trait of CDRX.[57,58] The formation of HAGBs occurs when subgrains generated during DRV processes gradually rotate and widen their misorientation angles under applied strain, a mechanism referred to as CDRX.[19,59] Notably, CDRX necessitates DRV as a prerequisite. In essence, it is implied that the presence of cellular solidification structures in the as-built state, characterized by walls entangled with dislocations, could be susceptible to DRV during the initial stage of hot compression processes.[60] This could result in the evolution of subgrains as new structures to reduce the accumulation of stored energy in the form of dislocations. Simultaneously, this process could coincide with dynamic recrystallization through a discontinuous mechanism during hot deformation.

Essentially, a portion of the stored energy in the as-built state is generated during the LPBF process due to its high solidification rate and the formation of metastable cellular structures. This energy can be released as the temperature increases during the subsequent hot deformation process. As this phenomenon unfolds within the micrograins, the micrograins are also influenced by the hot deformation processes and the strains induced during this process. Therefore, recrystallization in the form of DDRX could also occur simultaneously along HAGBs. It is thereby implied that both DRV–CDRX and DDRX processes could be taking place during the hot deformation process in the as-built parts.

Additionally, the creation of subgrains in metallic components fabricated by LPBF serves as substantially stronger impediments to dislocation mobility when compared to the grain boundaries found in wrought alloys. Literature discussions suggest that subgrain boundaries (LAGBs) act as robust impediments to dislocation motion, as evidenced by a larger Hall–Petch constant for metallic component fabricated by LPBF compared to nanostructured wrought materials dominated by HAGBs.[60] This enhanced strength may stem from the reinforcing effects introduced by dislocation cells during the DRV process. This entails the reorganization of densely packed dislocations into LAGBs, as well as the movement of mobile dislocations sliding along specific crystallographic planes, resulting in LAGBs acting as formidable barriers. Consequently, the formation of pores or cracks could occur alongside the cellular structures in LPBF samples subjected to hot deformation. This phenomenon, observed in B_{550} samples, confirms the accumulation of strains around cellular structures as potent obstacles to dislocation movements, potentially leading to localized strain and ultimately resulting in the formation of pores or cracks.

The restoration phenomenon during the hot deformation of heat-treated samples (H samples) is also investigated to identify differences in DRV/DRX behavior between LPBF heat-treated samples and their counterparts in the as-built state (B samples). IPF map of the H_{300} sample, which was hot compressed at 300 °C, is shown in Figure 8(a) with Area 1, which is marked on it. The enlarged view of Area 1, along with its associated IQ and KAM maps, is also presented in Figure 8(b). Furthermore, the IPF map of a region indicated in the IQ map of Area 1 is also magnified and depicted in Figure 8(b) labeled as Location 1. The KAM maps of Area 1 (Figure 8(b)), which provide a qualitative representation of local strain distribution in a structure,[61] suggest that the low local strain is accumulated in Area 1. Moreover, fine grains, associated with DRX, can be observed in Location 1, located within Area 1.

The low KAM values of Area 1 could confirm the relaxation of stored energy in Area 1 associated with the occurrence of softening, especially the formation of new fine recrystallized grains. The formation of fine, new recrystallized grains in certain areas of the H_{300} sample could indicate the occurrence of a partial DRX process during the hot deformation of this sample. However, it is noteworthy that the average value of grain size of the H_{300} sample (Figure 4(h)) is higher than the average grain size of the H_0 sample and the remaining hot-deformed heat-treated samples. The H_{300} sample is hot-deformed at the lowest temperature among the other samples, and the reduction in its flow stress is the least among the other hot-deformed heat-treated samples compared to the H_0 sample (Figure 3(c)). This behavior could be attributed to the effect of temperature on the critical strain required to trigger the DRX process. The lower temperatures, at a constant strain rate, resulted in a greater critical strain required to initiate DRX. Therefore, the critical strain (ε_c) required to induce DRX in the H_{300} sample is higher than that of

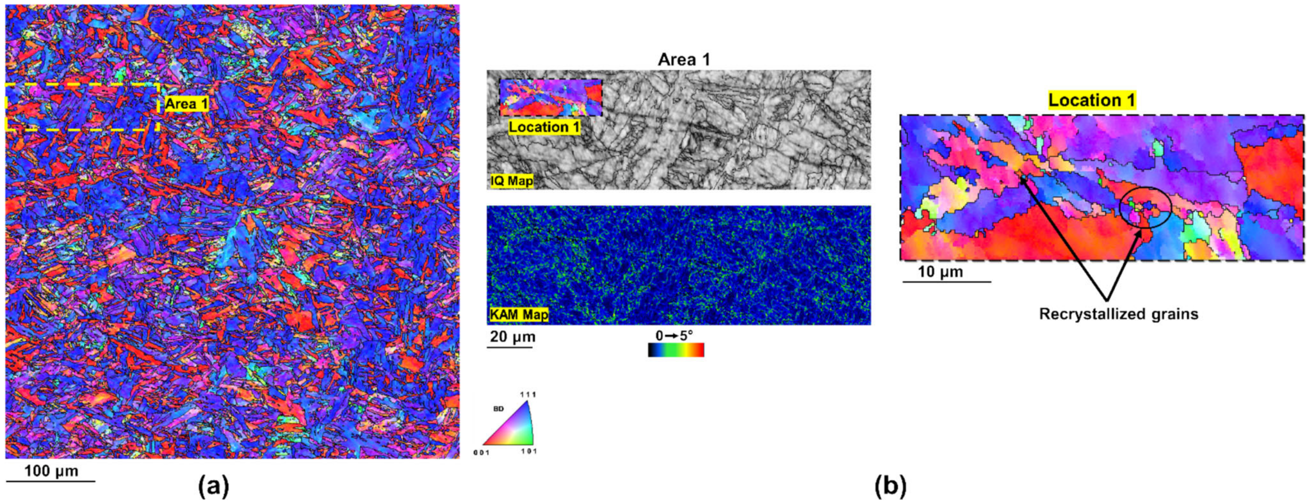

Fig. 8—(*a*) IPF-BD map of H_{300} sample with Area 1 marked on it, and (*b*) IQ and KAM maps of Area 1, with enlarged view of location 1 marked on Area 1.

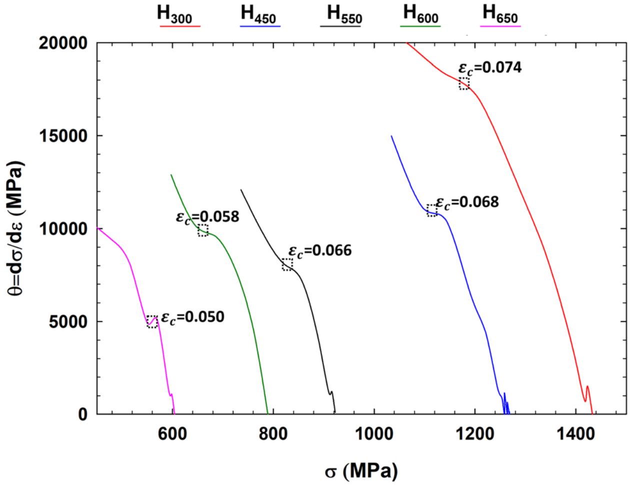

Fig. 9—Plot $\frac{d\sigma}{d\varepsilon}$ *vs.* σ up to the peak points of the true stress–strain curves at various hot compression temperature with strain rates 1 s^{-1} for the heat-treated samples (H samples).

the other heat-treated samples. This is determined by analyzing the work hardening plots ($\theta = \frac{d\sigma}{d\varepsilon}$) *vs.* the true stress (σ), calculated from the true stress–strain curves obtained during the hot compression tests, as illustrated in Figure 9.

In other words, the critical condition for the initiation of DRX is estimated when the absolute value of $\left|-\frac{d\theta}{d\sigma}\right|$ reaches the minimum, corresponding to an inflection point in $\theta = \frac{d\sigma}{d\varepsilon}$ *vs.* the true stress (σ).[62] The second derivative of the $\theta = \frac{d\sigma}{d\varepsilon}$ *vs.* the true stress (σ) was calculated to identify the points where it equals zero and changes sign, indicating a shift in concavity for detecting the inflection points. Accordingly, the fraction of new DRX grains decreases when the critical strain is high. It is also suggested that the H_{300} sample has the highest fraction of very low-angle grain boundaries compared to the rest of the heat-treated samples (Figure 4(i)). This observation could be partly attributed to the formation of substructures due to DRV and the existence of strains within the hot compression. Consequently, the lower tendency for DRX in the H_{300} sample in contrast to the other H samples, along with the presence of elongated deformed grains, led to a rise in the average value of grain size of the hot-deformed sample at 300 °C compared to H_0 and the remaining hot-deformed H samples. Furthermore, the lower tendency of the H_{300} compared to the other hot-deformed H samples could be linked to the presence of the ordered β-NiAl phase with a B_2 (CsCl) structure. The relevant bright-field (BF) micrograph, with diffraction patterns inserted, along with the corresponding dark-field (DF) image from the heat-treated CX sample, is shown in Figure 10. A DF-TEM micrograph, taken from one of the superlattice reflections (labeled "B") associated with the β-NiAl precipitates in the diffraction pattern (Figure 10), clearly reveals the fine precipitates of β-NiAl in the matrix of the solution-annealed and aged (heat-treated) CX sample. Therefore, the microstructure of the heat-treated specimens includes β-NiAl precipitates, which could have a significant impact on the restoration process during the hot compression tests.

To comprehend the interactions between dynamic restoration mechanisms such as DRX and dynamic microstructure evolutions, including the reversion of austenite and precipitation/dissolution of nanoscale particles, the solid-state phase transformation temperatures were measured using dilatometry results obtained during continuous heating, as depicted in Figure 10(c). A representative plot of $\Delta L/L_0$ *vs.* temperature for the as-built LPBF CX sample at a heating rate of 5 °C/s is depicted in Figure 1(c).

The results of the dilatometry experiment confirmed that aging at temperatures between 480 °C and 570 °C led to the evolution of NiAl precipitates in the martensitic matrix of CX stainless steel. Moreover, the hot deformation process could expedite the dissolution of NiAl precipitates at temperatures higher than 570 °C.

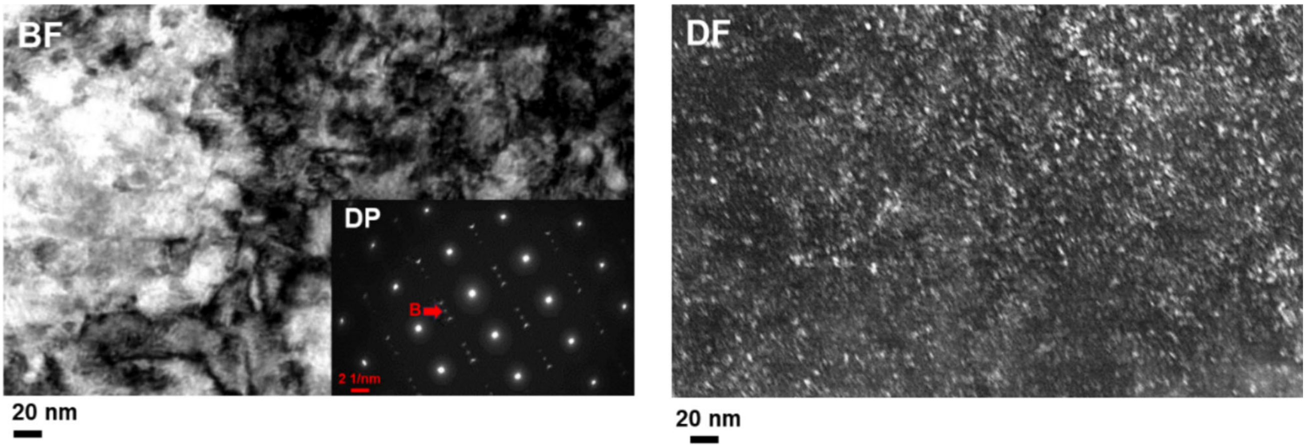

Fig. 10—TEM bright-field micrograph with an inserted diffraction pattern and a dark-field image showing the precipitate morphology in LPBF CX stainless steel specimens after heat treatment. The dark-field image is obtained from the superlattice spots indicated by "B" in the diffraction pattern.

Considering that the hot compression tests involved an approximate 50 °C increase in the temperature of the samples, the effective temperatures during deformation are approximately the hot-deformed temperatures plus 50 °C. Consequently, the H_{550}, H_{600}, and H_{650} samples, which underwent hot deformation at 550 °C, 600 °C, and 650 °C, are susceptible to the dissolution of NiAl in their matrix. Accordingly, it is implied that the dissolution of the precipitates could occur within the H_{550}, H_{600}, and H_{650} samples, while NiAl precipitates could remain unchanged within hot deformation at 300 °C and 450 °C in H_{300} and H_{450} samples, respectively. The presence of nanoscale NiAl precipitates in H_{300} and H_{450} samples could exert a notable pinning influence on the movements of both low and high-angle grain boundaries, thereby impeding both initiation and the following growth of recrystallized grains.[63]

It is evident from Figure 3(b) that deformation at high temperatures significantly influences the flow stress. Samples subjected to hot deformation at temperatures exceeding 450 °C exhibited a higher reduction in flow stress compared to the RT sample of H samples. The reduction in the peak flow stress for the H_{550}, H_{600}, and H_{650} samples, in comparison to the ultimate strength of the RT sample, is approximately 50, 55, and 65 MPa, respectively. In contrast, the H_{300} sample showed a reduction of about 18 MPa in comparison to the RT sample. The greater reduction in flow stress for the H_{550} and H_{650} samples, along with the greater refinement of their grains compared to the H_0 and H_{300} samples, indicates a higher propensity for DRX processes. This results in a higher fraction of DRX within the hot deformation.

To gain a comprehensive understanding of the restoration phenomena on heat-treated hot-deformed LPBF samples, the development of recrystallization and the identification of possible sites for the nucleation were also estimated using microstructural partitioning of the samples by considering the GOS metric and considering recrystallized grains as having an average GOS value $\leq$ 1deg. Additionally, a size criterion was applied, where grains were considered valid only if they met the minimum requirement of ≥ 5 pixels per grain.

Accordingly, the IPF-BD maps of the portioned microstructure of H_{550} and H_{650} samples are depicted in Figures 11(a) and (b). Additionally, the grain size distribution of the partitioned structure, which indexes the possible recrystallized grains, is also displayed in Figure 11(c). It is clear from Figure 11(a) that a majority of the recrystallized grains in the H_{550} are in the early stage of growth, whereas the recrystallized grains in the H_{650} appear to be fully recrystallized and grown. The evolution of the recrystallized grain size distribution for the H_{550} and H_{650} samples reveals a notable difference between them. It is observed that the average peak of the grain size distribution shifts toward elevated values and widens for H_{650} compared to those of the H_{550}. The average size of recrystallized grains for the H_{550} sample is approximately 0.3 μm, whereas it is about 1.6 μm for the H_{650} sample.

Two key parameters are of crucial importance during the restoration processes occurring during hot deformation in heat-treated samples: (i) the evolution/dissolution of nanoscale NiAl precipitates and (ii) the temperature, both of which affect the migration of high-angle grain boundaries. It is noted that the recrystallized grain growth is affected by the HAGBs migration, and the growth kinetics are strongly influenced by the temperature and drag pressure induced by the nanoscale precipitates.

Accordingly, the hot deformation at 550 °C applied to the H_{550} sample could result in a deformation-induced temperature rise. This was corroborated by measuring a temperature rise of at least 50 °C in all specimens which were hot deformed. This increment of the temperature could completely or partially dissolve the nanoscale precipitates.

The transformation temperatures occurring during the heating phase of the hot compression process are more clearly observed in the derivatives of the $(\Delta L/L_0)$ *vs.* temperature plot, as shown in Figure 12(a). The tangent intersection principle was applied to the

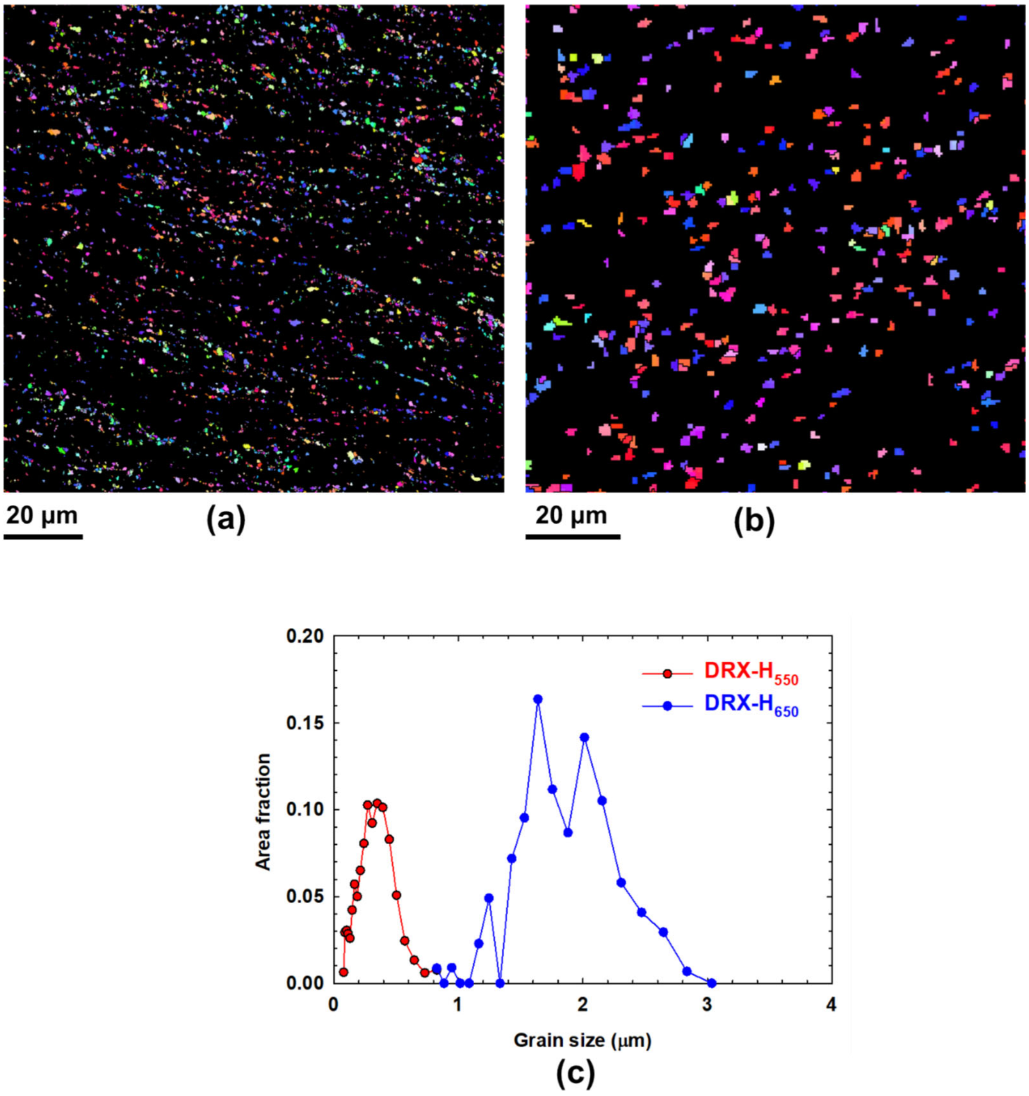

Fig. 11—Partitioned microstructure to recrystallized grains for (*a*) H_{550}, (*b*) H_{650} sample, and (*c*) grain size distribution plot of recrystallized grains in H_{550} and H_{650} samples.

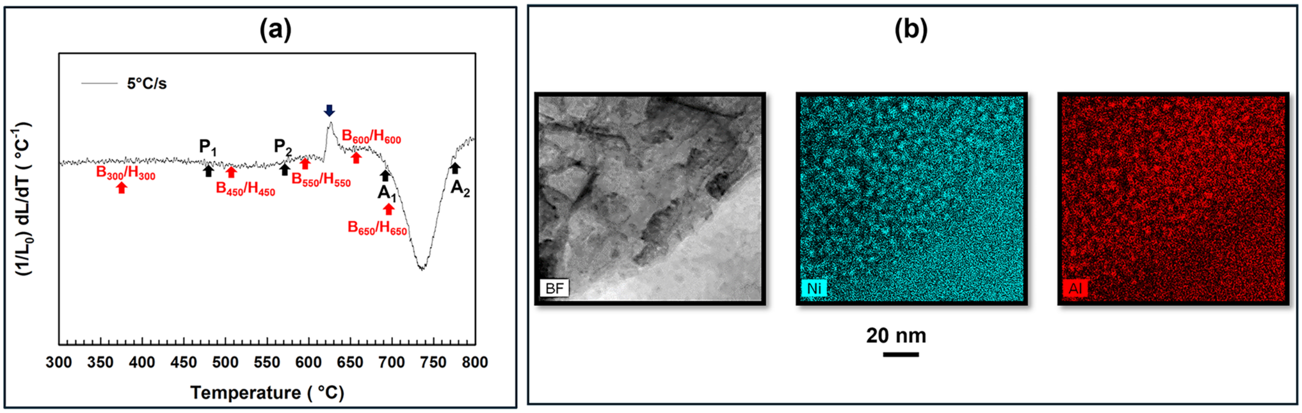

Fig. 12—(*a*) $(1/L_0)$ dL/dT *vs.* T for the heating rate within the hot compression process (5 °C/s), and (*b*) bright-field STEM micrograph obtained from the as-built CX SS sample continuously heated into 600 °C, and the corresponding EDS elemental maps of Ni and Al (Color figure online).

derivative plot (Figure 12(a)) at a 5 °C/s heating rate to determine the transformation temperatures. The positions of the precipitation start temperature (P_1) and precipitation finish temperature (P_2), as well as the austenite start temperature (A_1) and austenite finish temperature (A_2), are marked with black arrows in Figure 12(a). Additionally, the locations of the hot compression temperatures, considering deformation-induced temperature rise, are indicated with red arrows in Figure 12(a). Additionally, the ferromagnetic-to-paramagnetic transformation of the α phase is observed as a slight change in slope or a spike in the curves, as indicated by the blue arrows in Figure 12(b). According to the dilatometry results shown in Figure 12(a), hot compression at 550 °C leads to a temperature drop to 600 °C in the $(1/L_0)$ $\mathrm{d}L/\mathrm{d}T$–temperature plot, which is higher than P_2, suggesting the dissolution of precipitates. Nevertheless, TEM observations of the LPBF sample, subjected to continuous heating up to 600 °C, revealed the existence of nano-sized precipitates, as depicted in Figure 12(b). Hence, it is suggested that hot compression at 550 °C likely accelerates the dissolution of NiAl precipitates. However, some residual precipitates may persist, potentially impeding the recrystallization and growth of the recrystallized grains. In contrast, for the H_{650} sample, hot compression at 650 °C resulted in a specimen temperature of approximately 700 °C, surpassing the NiAl solvus temperature and reaching the temperature for the reversion of austenite (A_1), as shown in Figure 12(a). Additionally, elevated temperatures during constant strain rate hot deformation may boost the grain boundary mobility, and the higher temperatures contributed to a lower critical strain for the initiation of dynamic recrystallization. As a result, hot deformation of the heat-treated LPBF sample at 650 °C is expected to diminish barriers to the nucleation and growth of DRX grains. This occurs through the dissolution of NiAl precipitates and the increased mobility of high-angle grain boundaries, thereby fostering a greater tendency for DRX grain growth in comparison to those formed in the H_{550} sample.

D. *Effect of Nanoscale NiAl Precipitates on Restoration Process*

Figure 13 illustrates a scheme of the restoration mechanisms on hot-deformed LPBF parts in both the as-built condition and after undergoing a heat-treatment process. The pinning forces applied through NiAl particles on the movement of grain boundaries are also depicted in Figure 13. The presence of superlattice nanoscale NiAl precipitates in the H samples could impede both dynamic recovery/recrystallization and the DRX grain growth. In simpler terms, nanoscale NiAl particles might influence dynamic recovery by either anchoring individual dislocations, thereby impeding the initial development of low-angle boundaries, or by hindering the expansion of subgrains. Furthermore, the net driving pressure for DRX and grain growth (P) is also affected by a balance between the driving pressure for growth (P_D) and both Zener pinning pressure (P_Z) and the retarding pressure due to boundary curvature (P_C) in the very early stages of nucleation,[63] as follows:

$$P = P_D - P_Z - P_C = \alpha \Delta\rho G b^2 - \frac{3f\gamma}{2r} - \frac{2\gamma}{R}\dot{s}, \qquad [13]$$

where α denotes geometric constant, G presents the shear modulus, b is the Burgers vector, R is the radius of subgrain or radius of nucleus, and $\Delta\rho$ represents the alteration in dislocation density linked to the migration of the recrystallization front into the deformation substructure, r notes the radius of the pinning particles, and f is the volume fraction of particles. Also, γ in J/m^2 is surface tension of a grain boundary. It is evident from Eq. [9] that recrystallized grain growth requires a positive value of P, and the advancement of recrystallization will heavily rely on the dispersion parameter's value $\left(\frac{f}{r}\right)$.

According to Humphreys and Hatherly,[64] the nucleation of DRX will be inhibited when $\frac{f}{r} > 0.15\mu\mathrm{m}^{-1}$ and the recrystallization nucleus growth is hindered for certain values of $0.2\mu\mathrm{m}^{-1} < \left(\frac{f}{r}\right) < 0.6\mu\mathrm{m}^{-1}$. The neutron diffraction analyses of the LPBF CX SS specimens after heat treatment in our group research showed that the volume fraction of nanoscale NiAl precipitates dispersed after aging at 530 °C for a soaking time of 3 hours is approximately 0.01. Our previous results on heat-treated LPBF CX SS indicated the formation of coherent nanoscale NiAl particles with a size lower than 10 nm.[65] Therefore, the value of $\left(\frac{f}{r}\right)$ for these particles falls within the range of the dispersion parameter known for retarding the DRX. The impeding impact of nanoscale NiAl particles could be confirmed for the hot-deformed samples at 300 °C and 450 °C, which exhibited a larger grain size and a lower reduction in flow stress compared to the heat-treated samples deformed at temperatures higher than 450 °C. According to the dilatometry results presented in Figures 1(c) and 12(a), the dissolution of NiAl particles could commence at temperatures higher than 570 °C. Additionally, an increment of about 50 °C is also observed within hot deformation processes due to strain-induced temperature rise. Consequently, the hot-deformed samples at temperatures higher than 450 °C are within the temperature range for resolving the precipitates as shown in Figure 12(a). It is noted that heat-treated samples deformed at 550 °C, 600 °C, and 650 °C displayed a lower grain size as well as a higher reduction in flow stress than H_{300} and H_{450} samples due to the partial and complete dissolution of nanoscale particles.

Although the presence of nanoscale precipitates could impede the restoration processes in the samples which were heat treated, it appears that the retardation effect of cellular solidification subgrains during hot deformation at temperatures beneath 550 °C could be greater than the impeding effects of the nanoscale precipitates. The lower reduction in flow stresses in B_{300} and B_{450} samples compared to the H_{300} and H_{450} samples could confirm this behavior. The partitioning of heavy solute elements such as Cr and Ni could occur on the cell

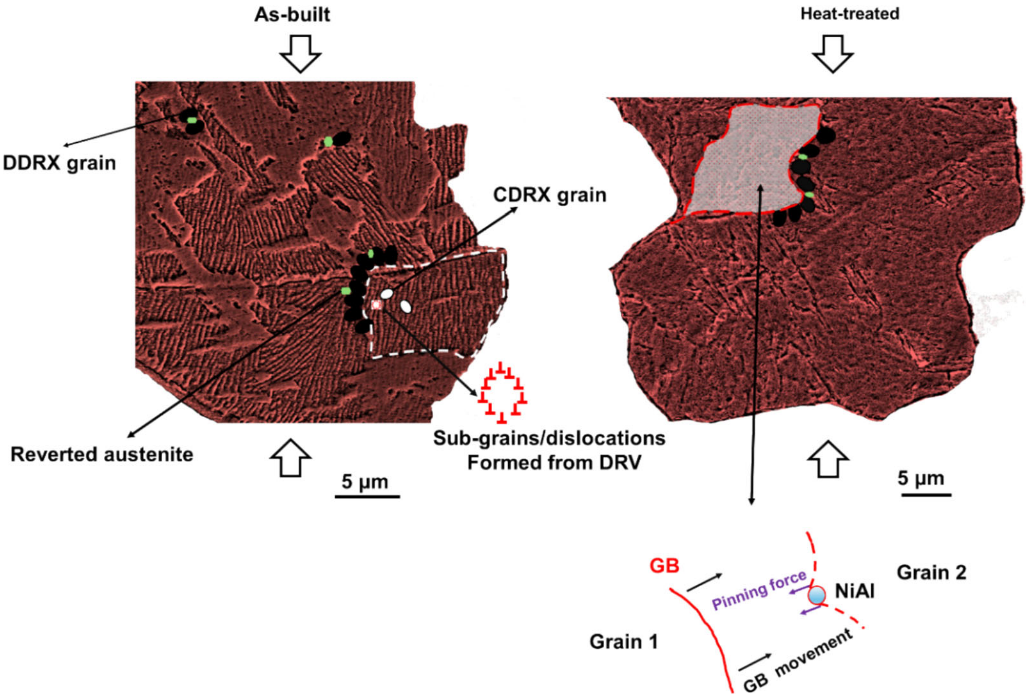

Fig. 13—A scheme of the restoration phenomena during hot deformation process on LPBF CX SS in the as-built state and after heat-treatment process.

boundaries as a result of segregation. Indirect evidence indicates that partitioned elements at the cell walls play a role in stabilizing the cellular network through pinning effects.[7] Indeed, the movement of grain boundaries could be restricted by the drag pressure applied through the solute elements entangled with the cellular solidification walls, resulting in a Zener pinning effect. This effect could lead to the retardation of the restoration processes in the as-built specimens. Nevertheless, the partial and complete de-structuring of cellular solidification subgrains at temperatures higher than 550 °C in the as-built samples, as well as the dissolution of nanoscale NiAl precipitates in the heat-treated samples, leads to a very similar deformation behavior of both the as-built and annealed LPBF samples. Consequently, the values of flow stresses for B_{550}, B_{600}, B_{650}, and their counterparts, including H_{550}, H_{600}, and H_{650}, would be close to each other, as the differences of σ_P in the as-built state and its counterpart after heat treatment reach approximately 51, 3, and 7 MPa for deformed samples at 550 °C, 600 °C, and 650 °C, respectively.

As schematically presented in Figure 13, the appearance of reverted austenite also occurred within the hot compression process at temperatures higher than 550 °C. Although the martensite-to-austenite transformation temperature is estimated from the dilatometry results to be in the range of 700 °C to 770 °C at a heating rate of 5 °C/s, the evolution of reverted austenite in B_{550} samples as well as in the H_{550} sample implies that the restoration processes during hot deformation push the reversion of martensite phase to austenite to lower temperatures than predicted by the dilatometry results. This behavior could be attributed to providing additional grain boundaries and accelerating element diffusion through the restoration mechanism, which increases the driving force for the martensite-to-austenite reversion phenomena.

E. *DRV/DRX Mechanisms*

In the context of restoration mechanisms during the hot deformation of LPBF CX parts in the as-built condition and after heat-treatment process, EBSD-based microstructure analyses have revealed the presence of elongated grains and fine recrystallized grains. The volume fraction of dynamically recrystallized (DRX) grains appears to be lower than that of the initial grains. This indicates that the softening mechanism observed during the hot deformation of LPBF parts, in the as-built state and after undergoing heat-treatment process, is a combination of DRV and DRX processes. Concurrently, a significant density of dislocations could be produced within both the LPBF process and the subsequent post-hot compression process. This dislocation density can be mitigated through the cross-slip of screw dislocations, climbing of edge dislocations, and opposing dislocation motions under the DRV process. Also, when the combination of strain hardening and recovery reaches a point where it can no longer accommodate additional immobile dislocations, the strain reaches a critical threshold. At this juncture, dynamic recovery ceases, and the onset of DRX occurs to alleviate the remaining accumulated stored energy generated during the thermomechanical processes.

In the as-built state of samples, the presence of cellular subgrains could affect the restoration mechanism. In these samples, when the DRV process is active, either as a standalone process or as a precursor to

CDRX, the dislocation tangles within cell walls become more orderly, forming regular dislocation networks or Low-Angle Grain Boundaries (LAGBs). Consequently, as recovery progresses, the number of dislocations in the cell interiors diminishes. This leads to the cells transforming into subgrains bordered by LAGBs. The shift from dislocation cells to LAGBs entails the elimination of excess dislocations and the reorganization of the remaining ones into LAGBs. Furthermore, as the subgrains formed during DRV processes undergo progressive rotation and experience an increase in misorientation angles caused by the applied strain, high-angle grain boundaries (HAGBs) emerge. This mechanism is referred to as CDRX, and its representation is depicted schematically in Figure 13.

In essence, the observation revealed the destruction of cellular structures in the as-built samples that underwent hot deformation at temperatures exceeding 550 °C. This destruction implies a conversion of cellular structures into fine recrystallized grains through a combination of DRV and CDRX processes. The gradual increase in misorientation angles of subgrains, a result of the recovery process, led to the formation of HAGBs as fine recrystallized grains, causing the disappearance of cellular structures in the as-built samples. It is noteworthy that recrystallized grains also nucleated at initial grain boundaries, forming a characteristic necklace microstructure, indicative of the microstructural features of DDRX mechanism. Consequently, it can be inferred that the recrystallization mechanism in the as-built samples during the hot deformation process is concurrent in both CDRX and DDRX forms. On the other hand, evidence of CDRX was not detected in the H samples. However, the observation of the formation of a necklace microstructure in these samples indicates that the dominant dynamic recrystallization mechanism in the heat-treated samples is the DDRX process.

F. *Development of SBs*

Moreover, the identification of flow localization regions in the form of SBs was detected in the hot-deformed samples at temperatures of 300 °C and 450 °C, encompassing B_{300}, B_{450}, H_{300}, and H_{450} samples. However, no apparent indication of SBs was found in the hot-compressed samples at temperatures exceeding 450 °C. The occurrence of SBs at lower hot deformation temperatures may be attributed to the development of inhomogeneous deformation in regions with a high concentration of strain. Conversely, elevating the hot deformation temperature beyond 450 °C could mitigate flow localization by inducing higher ductility, resulting in a more uniform deformation. Furthermore, the presence of nanoscale NiAl precipitates could contribute to the initiation of SBs. These nanoscale NiAl precipitates possess a superlattice structure, potentially elevating the flow stress to a level where dislocations slice through the precipitates instead of bending around them.[66] Hence, the shearing of particles and the possible disruption of the superlattice structure could trigger localized softening and promote strain localization. This phenomenon would significantly contribute to the emergence of localized flow and the creation of SBs.

During the hot deformation of the as-built samples at 450 °C, according to the dilatometry results shown in Figures 1(c) and 12(a), the evolution of β-NiAl precipitates with superlattice structure possibly occurs at this temperature. This is because the deformation work led to an increase in temperature of approximately 50 °C, which is adequate to bring the temperature of the sample within the range conducive to NiAl evolution. Additionally, nanoscale superlattice NiAl precipitates are present in the hot-deformed, heat-treated samples at 300 °C (H_{300}) and 450 °C (H_{450}). Thus, it is inferred that the development of NiAl precipitates occurred during hot compression in the B_{450} sample, as well as the presence of these nanoscale precipitates in the H_{300} and H_{450} samples, stimulates the initiation of SBs in these samples. The frequent shearing of the nanoscale precipitates results in local softening and strain localization, which induces the formation of highly localized flow areas in the form of SBs/ASBs. However, the nanoscale precipitates of NiAl are not likely to form during the heating and hot deformation process in the B_{300} sample. The occurrence of SBs in this specimen may be ascribed to localized deformation at the original grain boundaries. Ultimately, the strain localizations created either by the presence of NiAl precipitates or grain boundaries could cause localized heating, resulting in enhanced dislocation movement. This results in the accumulation of sufficient strain to nucleate bands of fine recrystallized grains or an extreme response to the localized strain in the form of the macroscopic SBs shown in Figure 4.

V. CONCLUSIONS

The hot compression behavior of martensitic precipitation-hardening stainless steel (CX SS) fabricated by the LPBF technique was studied in the temperature range of 300 °C to 650 °C, using a fixed strain rate of 1 s^{-1}. Additionally, selected samples underwent solution annealing and aging to observe the evolution of nanoscale precipitates of NiAl in their matrix. These treated samples were then subjected to hot compression under the same conditions as the as-built samples. Phenomenological constitutive equations and numerical analysis with the Finite Element Method (FEM) were employed alongside microstructural analyses to investigate the interactions among microstructural features. The study examined the roles of these features in the restoration processes, specifically DRX and DRV, as well as the formation of SBs. The primary conclusions of the research are outlined as follows:

- The comparison of flow stress between the as-built and heat-treated samples showed that restoration mechanisms are more delayed in the as-built state at temperatures below 550 °C. However, above 450 °C, both conditions exhibited similar deformation behavior, likely due to the partial or full dissolution of cellular structures in the as-built samples and the dissolution of nanoscale NiAl particles in the heat-treated samples.

- In the as-built samples, the gradual increase in subgrain misorientation due to recovery contributes to the formation of HAGBs and fine recrystallized grains through the CDRX mechanism. Additionally, recrystallized grains form along initial grain boundaries, producing a characteristic necklace microstructure associated with DDRX. In contrast, heat-treated samples, which lack cellular solidification structures, primarily exhibit the necklace microstructure as a result of the DDRX mechanism.
- SBs/ASBs were observed in samples hot-deformed below 550 °C, displaying high strain gradients in an X-shaped pattern. In contrast, samples deformed above 450 °C showed more uniform strain distribution with lower gradients and a rectangular shape, indicating more homogeneous plastic deformation. The formation of SBs/ASBs is influenced by lower temperatures and the presence of NiAl, both of which promote localized flow.

ACKNOWLEDGMENTS

We are grateful for the funding received from the Atlantic Canada Opportunities Agency (ACOA) for support under Atlantic Innovation Fund (AIF, Project Number 210414), and the Mitacs Accelerate Program (Grant Number IT10669). One of the authors (LAIK) acknowledges partial financial support from the AID4-GREENEST Project (AI Powered Characterization and Modelling for Green Steel Technology) funded by the Horizon Europe Research and Innovation Program (Grant Agreement No. 101091912).

CONFLICT OF INTEREST

The authors declare that they have no conflict of interest.

REFERENCES

1. A. Abrahams: *The Development of High Strength Corrosion Resistant*. PhD dissertation, The Pennsylvania State University, 2010.
2. L. Tan, D. Li, L. Yan, X. Pang, and K. Gao: *Mater. Sci. Eng. A*, 2023, vol. 873, p. 145062.
3. Y.R. Wen, A. Hirata, Z.W. Zhang, T. Fujita, C.T. Liu, J.H. Jiang, and M.W. Chen: *Acta Mater.*, 2013, vol. 61, pp. 2133–47.
4. A. Shahriari, M. Sanjari, M. Mahmoudiniya, H. Pirgazi, B. Shalchi Amirkhiz, L.A.I. Kestens, and M. Mohammadi: *Metall. Mater. Trans. A*, 2024, vol. 55A, pp. 1302–10.
5. I. Gibson, D. Rosen, and B. Stucker: *Additive Manufacturing Technologies: 3D Printing, Rapid Prototyping, and Direct Digital Manufacturing*, 2nd ed. Springer, New York, 2015, pp. 1–498.
6. T. DebRoy, H.L. Wei, J.S. Zuback, T. Mukherjee, J.W. Elmer, J.O. Milewski, A.M. Beese, A. Wilson-Heid, A. De, and W. Zhang: *Prog. Mater. Sci.*, 2018, vol. 92, pp. 112–224.
7. Y.M. Wang, T. Voisin, J.T. McKeown, J. Ye, N.P. Calta, Z. Li, Z. Zeng, Y. Zhang, W. Chen, T.T. Roehling, R.T. Ott, M.K. Santala, P.J. Depond, M.J. Matthews, A.V. Hamza, and T. Zhu: *Nat. Mater.*, 2017, vol. 17(1), pp. 63–71.
8. H. Zhang, M. Xu, Z. Liu, C. Li, P. Kumar, Z. Liu, and Y. Zhang: *Addit. Manuf.*, 2021, vol. 46, p. 102147.
9. D. Hu, Z. Guo, N. Grilli, A. Tay, Z. Lu, and W. Yan: *Int. J. Plast.*, 2024, vol. 177, p. 103981.
10. Y. Zhao, J. Chen, G. Zhao, Z. Yu, X. Ren, Q. Wang, W. Xu, S. Ren, and X. Qu: *Metall. Mater. Trans. A*, 2024A, vol. 2024A, pp. 1–19.
11. Z.K. Teng, M.K. Miller, G. Ghosh, C.T. Liu, S. Huang, K.F. Russell, M.E. Fine, and P.K. Liaw: *Scripta Mater.*, 2010, vol. 63, pp. 61–64.
12. S. Anishetty, T. Bera, J.D. Majumdar, and I. Manna: *Metall. Mater. Trans. A*, 2024, vol. 55A, pp. 3982–4000.
13. Y.M. Wang, T. Voisin, J.T. McKeown, J. Ye, N.P. Calta, Z. Li, Z. Zeng, Y. Zhang, W. Chen, T.T. Roehling, R.T. Ott, M.K. Santala, P.J. Depond, M.J. Matthews, A.V. Hamza, and T. Zhu: *Nat. Mater.*, 2018, vol. 17, pp. 63–70.
14. H. Zhang, C. Li, G. Yao, Y. Shi, and Y. Zhang: *Int. J. Plast.*, 2022, vol. 155, p. 103335.
15. H.K. Rafi, T.L. Starr, and B.E. Stucker: *Int. J. Adv. Manuf. Technol.*, 2013, vol. 69, pp. 1299–1309.
16. F.J. Humphreys and M. Hatherly: *Recrystallization and Related Annealing Phenomena*, Elsevier, Amsterdam, 2002, p. 520.
17. S. Mandal, A.K. Bhaduri, and V. Subramanya Sarma: *Metall. Mater. Trans. A*, 2011, vol. 42A, pp. 1062–72.
18. S. Mandal, M. Jayalakshmi, A.K. Bhaduri, and V. Subramanya Sarma: *Metall. Mater. Trans. A*, 2014, vol. 45A, pp. 5645–56.
19. S. Gourdet and F. Montheillet: *Acta Mater.*, 2003, vol. 51, pp. 2685–99.
20. M.E. Kassner and S.R. Barrabes: *Mater. Sci. Eng. A*, 2005, vol. 410–411, pp. 152–55.
21. U.F.H. Suhuddin, L. Rath, R.M. Halak, and B. Klusemann: *Mater. Charact.*, 2023, vol. 205, p. 113252.
22. S. Chen, K. Chen, G. Peng, X. Chen, and Q. Ceng: *J. Alloys Compd.*, 2012, vol. 537, pp. 338–45.
23. K. Huang, K. Marthinsen, Q. Zhao, and R.E. Logé: *Prog. Mater. Sci.*, 2018, vol. 92, pp. 284–359.
24. D. Mandal and I. Baker: *Acta Mater.*, 1997, vol. 45, pp. 453–61.
25. R. Fu, Y. Liu, Z. Xiao, Y. Huang, and H. Li: *J. Mater. Res. Technol.*, 2023, vol. 27, pp. 3259–73.
26. W. Li, J. Liu, Y. Zhou, S. Li, S. Wen, Q. Wei, C. Yan, and Y. Shi: *J. Alloys Compd.*, 2016, vol. 688, pp. 626–36.
27. Z. Liu, Y. Yang, Y. Xiao, H. Lei, C. Yang, Z. Liu, Q. Zhao, and C. Song: *Mater. Des.*, 2024, vol. 239, p. 112761.
28. E. Mirkoohi, H.C. Tran, Y.L. Lo, Y.C. Chang, H.Y. Lin, and S.Y. Liang: *Int. J. Adv. Manuf. Technol.*, 2020, vol. 107, pp. 4159–72.
29. H.E. Sabzi, N.T. Aboulkhair, X. Liang, X.H. Li, M. Simonelli, H. Fu, and P.E.J. Rivera-Díaz-del-Castillo: *Mater. Des.*, 2020, vol. 196, p. 109181.
30. J. Wang, R. Zhu, Y. Liu, and L. Zhang: *Adv. Powder Mater.*, 2023, vol. 2, p. 100137.
31. S.H. Sun, T. Ishimoto, K. Hagihara, Y. Tsutsumi, T. Hanawa, and T. Nakano: *Scripta Mater.*, 2019, vol. 159, pp. 89–93.
32. J. Yang, J. Han, H. Yu, J. Yin, M. Gao, Z. Wang, and X. Zeng: *Mater. Des.*, 2016, vol. 110, pp. 558–70.
33. F.C. Pinto, L.S. Aota, I.R. Souza Filho, D. Raabe, and H.R.Z. Sandim: *J. Mater. Sci.*, 2022, vol. 57, pp. 9576–98.
34. E. de Sonis, S. Dépinoy, P.F. Giroux, H. Maskrot, L. Lemarquis, O. Hercher, F. Villaret, and A.F. Gourgues-Lorenzon: *Mater. Charact.*, 2022, vol. 194, p. 112370.
35. F. Chen, H. Zhu, W. Chen, H. Ou, and Z. Cui: *Int. J. Plast.*, 2021, vol. 145, p. 103064.
36. J. Zhang, C. Wu, Y. Peng, X. Xia, J. Li, J. Ding, C. Liu, X. Chen, J. Dong, and Y. Liu: *J. Alloys Compd.*, 2020, vol. 835, p. 155195.
37. G. Chen, L. Chen, G. Zhao, C. Zhang, and W. Cui: *J. Alloys Compd.*, 2017, vol. 710, pp. 80–91.
38. T. Mirzaie, H. Mirzadeh, and J.M. Cabrera: *Mech. Mater.*, 2016, vol. 94, pp. 38–45.
39. Z. Zhou, H. Gong, J. You, S. Liu, and J. He: *Mater. Today Commun.*, 2021, vol. 28, p. 102507.
40. Y.C. Lin, M.S. Chen, and J. Zhong: *Comput. Mater. Sci.*, 2008, vol. 42, pp. 470–77.

41. A. Shahriari, L. Khaksar, A. Nasiri, A. Hadadzadeh, B.S. Amirkhiz, and M. Mohammadi: *Electrochim. Acta*, 2020, vol. 339, p. 135925.
42. P. Yang, C. Liu, Q. Guo, and Y. Liu: *J. Mater. Sci. Technol.*, 2021, vol. 72, pp. 162–71.
43. F. Zhang, D. Liu, Y. Yang, C. Liu, Z. Zhang, H. Wang, and J. Wang: *J. Alloys Compd.*, 2020, vol. 817, p. 152773.
44. Y. Wang, W.Z. Shao, L. Zhen, and B.Y. Zhang: *Mater. Sci. Eng. A*, 2011, vol. 528, pp. 3218–27.
45. D. Caillard and J.-L. Martin: *Thermally Activated Mechanisms in Crystal Plasticity*, vol. 8, Elsevier, Amsterdam, 2003, pp. 13–53.
46. S.I. Oh, S.L. Semiatin, and J.J. Jonas: *Metall. Trans. A*, 1992, vol. 23, pp. 963–75.
47. R. Ebrahimi and A. Najafizadeh: *J. Mater. Process. Technol.*, 2004, vol. 152, pp. 136–43.
48. M. Sanjari, M. Mahmoudiniya, H. Pirgazi, S. Tamimi, M.H. Ghoncheh, A. Shahriairi, A. Hadadzadeh, B.S. Amirkhiz, M. Purdy, E.G. de Araujo, L. Kestens, and M. Mohammadi: *Mater. Charact.*, 2022, vol. 192, p. 112185.
49. W.S. Shin, B. Son, W. Song, H. Sohn, H. Jang, Y.J. Kim, and C. Park: *Mater. Sci. Eng. A*, 2021, vol. 806, p. 140805.
50. K.G. Prashanth and J. Eckert: *J. Alloys Compd.*, 2017, vol. 707, pp. 27–34.
51. J. Yan, Q.L. Pan, B. Li, Z.Q. Huang, Z.M. Liu, and Z.M. Yin: *J. Alloys Compd.*, 2015, vol. 632, pp. 549–57.
52. H.R. Ezatpour, M. Haddad Sabzevar, S.A. Sajjadi, and Y. Huang: *Mater. Sci. Eng. A*, 2014, vol. 606, pp. 240–47.
53. H. Huang, F. Jiang, J. Zhou, L. Wei, M. Zhong, and X. Liu: *J. Alloys Compd.*, 2015, vol. 644, pp. 862–72.
54. D. Jorge-Badiola, A. Iza-Mendia, and I. Gutiérrez: *Mater. Sci. Eng. A*, 2005, vol. 394, pp. 445–54.
55. C. Zheng and D. Raabe: *Acta Mater.*, 2013, vol. 61, pp. 5504–17.
56. P. Deng, H. Yin, M. Song, D. Li, Y. Zheng, B.C. Prorok, and X. Lou: *JOM*, 2020, vol. 72, pp. 4232–43.
57. Z. Yanushkevich, A. Belyakov, and R. Kaibyshev: *Acta Mater.*, 2015, vol. 82, pp. 244–54.
58. Z. Yanushkevich, S.V. Dobatkin, A. Belyakov, and R. Kaibyshev: *Acta Mater.*, 2017, vol. 136, pp. 39–48.
59. M. Tikhonova, R. Kaibyshev, and A. Belyakov: *Adv. Eng. Mater.*, 2018, vol. 20, p. 1700960.
60. H.E. Sabzi, E. Hernandez-Nava, X.H. Li, H. Fu, D. San-Martín, and P.E.J. Rivera-Díaz-del-Castillo: *Mater. Des.*, 2021, vol. 212, p. 110246.
61. K.A. Babu, Y.H. Mozumder, R. Saha, V.S. Sarma, and S. Mandal: *Mater. Sci. Eng. A*, 2018, vol. 734, pp. 269–80.
62. E.I. Poliak and J.J. Jonas: *Acta Mater.*, 1996, vol. 44, pp. 127–36.
63. P.A. Manohar, M. Ferry, and T. Chandra: *ISIJ Int.*, 1998, vol. 38, pp. 913–24.
64. F.J. Humphreys and M. Hatherly: *Recrystallization and Related Annealing Phenomena*, Elsevier, Amsterdam, 2012, pp. 1–497.
65. A. Hadadzadeh, A. Shahriari, B.S. Amirkhiz, J. Li, and M. Mohammadi: *Mater. Sci. Eng. A*, 2020, vol. 787, p. 139470.
66. M.C. Mataya, M.J. Carr, and G. Krauss: *Metall. Trans. A*, 1982, vol. 13, pp. 1263–74.